



# Investigations of pseudoshock dynamics in back pressured axisymmetric ducts

Michael Leonard<sup>1</sup>, Soumen Chakravarthy<sup>1</sup>, William Stramecky<sup>1</sup>  and Venkateswaran Narayanaswamy<sup>1</sup> 

<sup>1</sup>Department of Mechanical and Aerospace Engineering, North Carolina State University, Raleigh, NC, USA

**Corresponding author:** Venkateswaran Narayanaswamy, [vnaraya3@ncsu.edu](mailto:vnaraya3@ncsu.edu)

(Received 19 April 2024; revised 19 May 2025; accepted 11 July 2025)

The dynamics of self-excited shock train oscillations in a back pressured axisymmetric duct was investigated to deepen the understanding of the isolator/combustor coupling in high-speed propulsion systems. The test article consisted of an internal compression inlet followed by a constant area isolator, both having a circular cross-section. A systematic back pressure variation was implemented by using a combination of aerodynamic and physical blockages at the isolator exit. High bandwidth two-dimensional pressure field imaging was performed at 8 kHz repetition rate within the isolator for different back pressure settings. The acquisition rate was considerably higher than the dominant frequency of the shock train oscillations across the different back pressure settings. The power spectral density of the pressure fluctuations beneath the leading shock foot exhibited broadband low frequency oscillations across all back pressures that resembled the motions of canonical shock–boundary layer interaction units. A node in the vicinity of reattachment location that originated the pressure perturbations within the separation shock was also identified, which further ascertained that the leading shock low frequency motions were driven by the separation bubble pulsations. Above a threshold back pressure, additional peaks appeared at distinct higher frequencies that resembled the acoustic modes within the duct. However, none of the earlier expressions of the resonance acoustic frequency within a straight duct agreed with the experimentally observed value. Cross-spectral analyses suggested that these modes were caused by the shock interactions with upstream propagating acoustic waves that emanate from the reattachment location, originally proposed for transonic diffusers by Robinet & Casalis (2001) *Phys. Fluids* **13**, 1047–1059. Feedback interactions described using one-dimensional stability analysis of the shock perturbations by obliquely travelling acoustic waves (Robinet & Casalis 2001 *Phys. Fluids* **13**, 1047–1059) made

favourable comparisons on the back pressure threshold that emanated the acoustic modes as well as the acoustic mode frequencies.

**Key words:** high-speed flow, shock waves, turbulent boundary layers

---

## 1. Introduction

In typical high-speed propulsion systems that operate in dual ramjet and scramjet modes, an isolator (also called diffuser) section separates the inlet from the combustor (Sullins 1993; Heister & Pratt 1994; Gnani, Zare-Behtash & Kontis 2016). The isolator is often a simple constant area or a slightly diverging duct that functions to insulate the inlet shock system from the pressure changes that occur at the combustor entry due to heat release variations during the flight trajectory. This function is accomplished by the establishment of a shock train followed by a mixing process region within the isolator section whose length and topology naturally adjust to match the combustor entry pressure. Since the inception of the isolator concept, extensive research has been performed to optimally size the isolator for a given flight trajectory. These include analytical models for the pressure distribution along the isolator length (e.g. Waltrup & Billig 1973) that are validated by multiple experimental studies involving both measurement of relevant flow quantities as well as visualization of the pseudoshock within the isolator (e.g. Carroll & Dutton 1990; Sullins & McLafferty 1992; Carroll, Lopez-Fernandez & Dutton 1993; Weiss, Grzona & Olivier 2010), as well as an extensive body of computational simulations of the isolator flow field (Hsieh, Bogar & Coakley 1987). The progress made in the research area has been periodically reviewed by several works (Meier, Szumowski & Selerowicz 1990; Matsuo, Miyazato & Kim 1999; Gnani *et al.* 2016; Philippou, Zachos & MacManus 2024).

The early works of Oswatitsch (1944) and Ferri & Nucci (1951) showed that the shock train established within the isolator executes strong self-excited and forced oscillations under steady and unsteady back pressured operations, respectively. The severe detrimental outcomes of the shock train oscillations had prompted a large body of research over several decades to characterize the shock oscillations at different Mach numbers and unravel the mechanisms that drive these oscillations (Matsuo *et al.* 1999; Gnani *et al.* 2016; Huang *et al.* 2023; Philippou *et al.* 2024). The focus of the present work is to delineate the mechanisms that drive the self-excited oscillations of the shock train, which remains one of the unsolved problems (Gnani *et al.* 2016), and the literature on this topic is selectively reviewed. Ikui *et al.* 1974<sup>a,b</sup> performed some of the earliest systematic investigations to characterize the shock train oscillations in a rectangular duct at multiple Mach number and back pressure settings. With the help of schlieren imaging, the authors observed that the shock train motions exhibited a combination of highly periodic and random oscillations. Within the periodic oscillations, the authors observed a bimodal wall pressure power spectra with one band centred at 40 Hz and the other above 100 Hz. Yamane *et al.* (1984<sup>a</sup>) further observed that the lower frequency band occurred only beneath the leading shock foot of the pseudoshock. A similar bimodal spectrum of the shock train oscillations was also observed in transonic rectangular diffusers (Bogar, Sajben & Kroutil 1983). Some of the more recent works made higher time resolution wall pressure measurements and schlieren imagery of the shock train oscillations. Xiong *et al.* (2017) made wall pressure measurements along the top and bottom walls of the isolator. They reported that the leading shock foot exhibited broadband oscillations centred in the Strouhal number (based on interaction length) range of 0.01–0.03, without the

occurrence of strong periodic oscillations. Hou *et al.* (2020) observed that the shock foot oscillations continued to exhibit the broadband spectrum even in the presence of background waves from the isolator. In summary, the nature of the shock train oscillations depends quite strongly on the operating Mach number and the back pressure imposed on the duct.

Several works have made detailed studies on the spatiotemporal relationships that occur within the shock train to elucidate its driving mechanisms. Ikui *et al.* (1974*a*) observed that the leading shock train perturbations impact the downstream shock legs at progressively greater time delays. They developed a low flow model of shock train oscillation behaviour where they analysed the leading shock when it is perturbed by the incoming boundary layer perturbations. Based on the observations, the authors suggest that the shock oscillations are driven by the incoming boundary layer perturbations. The authors further attributed the 40 Hz band to the Helmholtz-resonator-type behaviour that emanated from the settling chamber located downstream of the duct and the 100 Hz to the pressure waves set up within the duct. Subsequently, Yamane *et al.* (1984*b*) made a detailed statistical analysis of the unsteady pressure datasets and found the occurrence of both upstream and downstream propagating pressure perturbations within the pseudoshock. Sugiyama *et al.* (1988) made high repetition rate schlieren imagery of the shock train oscillations within a rectangular duct and observed that the pseudoshock oscillations occurred in phase with the incoming boundary layer thickness variations. This led the authors to suggest that the oscillations are driven by the variations in the incoming boundary layer. The self-excited shock oscillations were also handled from a perspective of one-dimensional (1-D) stability analysis of the terminal shock wave interacting with the upstream propagating acoustic wave by Robinet & Casalis (1999, 2001). The authors implemented this analysis on Bogar *et al.* (1983) and demonstrated a better agreement between the computed and experimental frequencies of self-excited shock oscillations. Li *et al.* (2017) developed a low-order model for shock train oscillations. They suggested that the shock train oscillations can be divided into three contributions: first, that occurs from inherent shock wave dynamics; second, from the acoustic propagation of back pressure fluctuation; third, from the changing duct volume downstream of the lead shock as separated region changes in size. The time trace of the isolator duct pressure predicted with their model favourably compared with the experiments performed at inflow Mach 2.7 and Mach 1.8. Hunt & Gamba (2019) performed high repetition rate wall pressure measurements and velocimetry in an isolator duct that had a highly asymmetric inflow. Using cross-correlation and cross-coherence approaches, the authors identified a strong upstream acoustic wave propagation that emanated from the exit diffuser and fed oscillations of the leading shock of the shock train. Using the velocity fields within the shock train, they posited that the downstream propagation of the pressure perturbation likely caused by the convecting vortices that emanate from the shear layer of the separated flow downstream of the leading shock. Other than the influence from the separated flow within the top and bottom wall, the authors found a sizeable influence from the sidewall separation and corner separation at the intersection of the top/bottom and sidewalls of the duct. The additional influence from the sidewall and corner separations exacerbated the complexity of interactions that drive the pseudoshock motions, which can be understood only if the actual three-dimensional (3-D) flow field is considered. Morgan, Duraisamy & Lele (2014) conducted large-eddy simulations of a supersonic isolator duct. They showed that whereas the simulations that did not account for the sidewall separation resulted in a stable pseudoshock, including the sidewall separation demonstrated that the pseudoshock can no longer be sustained within the isolator and resulted in an unstart.

The complicated 3-D nature of the planar inlets germinated multiple efforts into axisymmetric isolators, which epitomizes a two-dimensional (2-D) flow field within the duct. Om, Viegas & Childs (1985) performed detailed experimental investigations of the surface pressure distribution and the boundary layer parameters within a circular duct subjected to a steady back pressure. Oh *et al.* (2005) conducted numerical simulations of the axisymmetric inlets with a nose cone spike. The authors conducted detailed investigations of the terminal normal shock response to upstream propagating acoustic waves, but took into account the aerodynamic flow field that emanates from the upstream shock train established within the inlet. More recently, Leonard & Narayanaswamy (2021) made a detailed experimental characterization of an axisymmetric inlet/isolator without the application of back pressure and observed aperiodic shock foot oscillations even with attached boundary layers.

Despite the progress made towards filling the knowledge on the mechanisms that drive the self-excited shock train oscillations, there are several fundamental gaps in our present understanding of the underlying physics. For example, it is not clear if there are certain back pressure thresholds for a given inlet/isolator that will emanate the periodic motions within the isolator duct. While there are a few studies where the shock train oscillations were investigated at different back pressures, all these works had a downstream subsonic flow that invariably resulted in a large separation scale across all back pressure settings. As such, no prior studies have investigated if there is a shift in the governing mechanisms of the shock train dynamics with changing back pressure. If there is indeed a shift, then this could have major implications on the approaches to controlling the shock train dynamics that can directly impact the engine safety. Similarly, it is clear that using planar diffusers poses a significant challenge to performing high-fidelity computations owing to the three dimensionality of the flow field within these diffusers. However, compared with planar diffusers, there are only very few experimental datasets on axisymmetric inlets that have comparatively lower flow field complexity. Obtaining validation quality datasets in an axisymmetric isolator can substantially augment the fidelity of the computational simulations of the isolator flows. These factors motivated the present study to be conducted in a canonical axisymmetric inlet/isolator, which epitomizes a 2-D design and also holds significant practical relevance in supersonic flight vehicles. The design of the inlet/isolator was made after extensive computational simulations of the flow development within the duct that was supplemented by experimental measurements of boundary layer profiles at specific streamwise locations within the duct. The resulting geometry was large enough to ensure that only a minimum fraction of the flow was covered by the viscous boundary layer prior to the shock train but is small enough to be tested in our wind tunnel facility.

An important challenge with conducting shock train dynamics experiments over a wide range of back pressure settings is that the shock train structure evolves with back pressure and get displaced to considerably different locations within the isolator, which poses a significant challenge with instrumenting a large number of pressure transducers at the exact locations beneath the shock train. Furthermore, all prior investigations have made point measurements of the pressure fields, which creates a lacuna in obtaining a comprehensive picture of the flow dynamics especially in complex 3-D flow fields of back pressured isolators that exhibit 2-D surface pressure variations across the isolator length and span.

The present work addresses the abovementioned limitations of the earlier works and seeks to elucidate the mechanisms that drive the shock train dynamics in axisymmetric isolators. Several salient features need to be highlighted that distinguish the present work from the prior work on this topic. The isolator succeeded an internal compression axisymmetric inlet, and the inlet/isolator test article was placed at zero incidence angle

to the wind tunnel flow. These factors provided a highly symmetric flow development within the isolator and a nearly 2-D mean flow entering the pseudoshock. The back pressure was varied by a significant range that caused the estimated separation scale to vary by over five folds. The range of back pressures also provided a nominally supersonic as well as a subsonic flow at the diffuser exit, which was absent in the earlier works. Finally, in a significant leap from pointwise pressure measurements of earlier works, 2-D unsteady surface pressure fields were obtained using high-bandwidth pressure-sensitive paints. The time resolution was sufficient to adequately resolve the leading and succeeding shock (called ‘trailing shock’) oscillations of the pseudoshock across all back pressure settings. Our team has made similar high-bandwidth surface pressure field imaging in external and internal flow fields, including inlet/isolator geometries, and the present work makes another novel application of high bandwidth pressure-sensitive paints (Funderburk & Narayanaswamy 2019*b*; Johnson *et al.* 2022*a,b*; Johnson & Narayanaswamy 2024; Puckett & Narayanaswamy 2024; Schram *et al.* 2025*a*).

The logic of exposition of this work is as follows. Section 2 describes the experimental set-up, and the measurement and simulation tools employed for this work. Section 3 describes the results, beginning from the basic flow field and pressure field characterizations across different back pressure settings in § 3.1. An effective back pressure is derived using Reynolds-averaged Navier–Stokes (RANS) calculations in § 3.4 that bridges the complex flow field at the isolator exit due to aerodynamic blockage to a simplified quantity that aid further discussions. Section 3.5 makes a deep dive into the dynamics of the shock train across different back pressures, and reveals the coexistence of both broadband and tonal oscillations in the shock train motions. Detailed statistical analysis is made in § 3.1 to elucidate the mechanisms that drive the shock train oscillations at different back pressure sections. We first use two-point cross-correlation approaches to identify the sources of pressure perturbations within the shock train and the cross-linking between the leading and trailing shock oscillations. Subsequently, we perform phase lag analysis in the frequency domain to delineate the sources of broadband and tonal shock train oscillations. This culminates with a theoretical treatment in § 3.2 on the origins of the tonal oscillations of the shock train. Further discussions on the competing mechanisms and the more recent evidences of their existence in applied axisymmetric inlet geometry are also discussed.

## 2. Experimental set-up

### 2.1. Test facility

Experiments were conducted in the North Carolina State University variable Mach number blowdown type supersonic tunnel capable of providing Mach 1.5 to 4.0 free stream. The test section had a square cross-section that measured  $150 \times 150$  mm and 650 mm in length. The experiments for the present study were conducted at Mach  $3.0 \pm 0.02$ . The total temperature,  $T_0$ , and stagnation pressure,  $p_0$ , for these tests were 300 K and 618 kPa, respectively, leading to a free stream static temperature,  $T_\infty$ , pressure,  $p_\infty$ , and velocity,  $u_\infty$ , of 107 K, 16.8 kPa and  $622 \text{ m s}^{-1}$ . The duration of a typical test run was 12 s of which steady state conditions were maintained over approximately 8 s. A PID (proportional integral derivative) hydraulic valve control maintained a steady stagnation pressure and ensured minimal variation (less than 3 %) in free stream conditions over the course of a run. More details of the facility and its operation can be obtained from the earlier works on this facility (Funderburk & Narayanaswamy 2019*a*; Pickles & Narayanaswamy 2020; Walz & Narayanaswamy 2023).



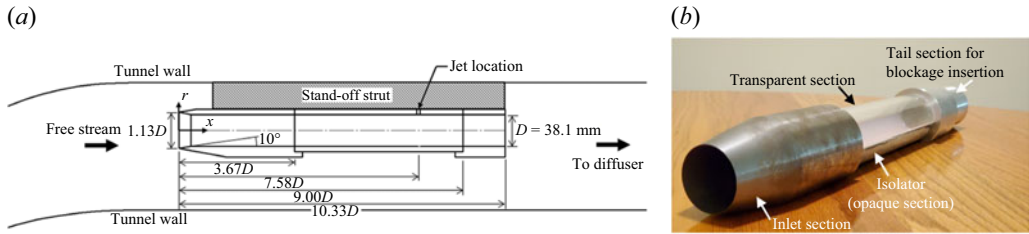


Figure 1. Schematic illustration of the test article set-up and its mounting to the wind tunnel (a), and a photograph of the inlet/isolator test article (b).

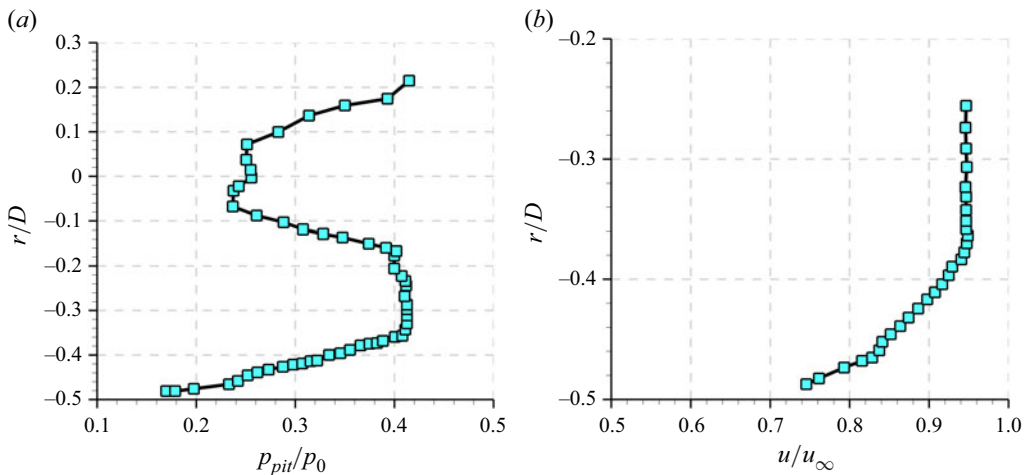


Figure 2. (a) Boundary layer profile of Pitot pressure to stagnation pressure ratio at  $x/D = 6.33$ , and (b) corresponding boundary layer velocity profile.

## 2.2. Test article

An axisymmetric inlet employed by Leonard & Narayanaswamy (2021) was used for the present investigations. The inlet was fitted with a constant-area circular cross-section isolator ( $D = 38.1$  mm). The schematic of the test article is presented in figure 1(a), and a photograph is presented in figure 1(b). As observed from figure 1(b), the test article consisted of a steel inlet, a transparent isolator section made of acrylic comprising the measurement domain from  $x/D = 4.0$  to  $x/D = 8.5$  and a steel isolator end section. The end section extended another  $1.83D$  downstream of the measurement domain and the isolator exit plane was located at  $x/D = 10.33$ . The steel inlet can be swapped out for different leading-edge angles; in this study, the results were obtained with a fixed  $10^\circ$  angle. The contraction ratio, defined as the ratio between the inlet capture area to the isolator cross-sectional area, was 1.28. For the discussions in this paper, the  $x$  location is defined as the streamwise distance downstream of the inlet entry plane (defined as  $x/D = 0$ ). The horizontal midplane of the isolator connects the azimuths  $\phi = -90^\circ$  and  $+90^\circ$  and extends between  $-0.5 \leq r/D \leq +0.5$ . Boundary layer profiles were reported in Leonard & Narayanaswamy (2021) at  $x/D = 6.33$  for the baseline configuration without back pressure. The profiles of the Pitot pressure normalized by the free stream stagnation pressure and the corresponding velocity profile are reproduced in figures 2(a) and 2(b),

respectively, from Leonard & Narayanaswamy (2021). A fine spatial resolution was maintained in the boundary profiles and the boundary layer profiles in the near wall regions that could not be measured were fitted with a model profile from Sun & Childs (1976). The estimates of 99 % boundary layer thickness, displacement thickness and momentum thickness are  $\delta/D = 0.113$ ,  $\delta^*/D = 0.048$  and  $\theta/D = 0.0081$ , respectively. The corresponding Pitot pressure measurements across the entire duct height revealed a symmetric profile about the model centreline as observed from figure 2(a) (Leonard & Narayanaswamy 2021).

### 2.3. Back pressure system

Two different back pressure systems were employed in the present study. The first system employed an aerodynamic blockage with a short rise time. At its maximum strength, this system was able to situate the leading shock of the shock train approximately at the midlength of the isolator section. The second system employed a physical blockage with a longer rise time. This system was capable of providing a significantly higher back pressure that was sufficient to unstart the inlet. For the present work, the physical blockage was set such that the shock train leading edge was situated approximately two diameters downstream of the isolator entry plane.

#### 2.3.1. Aerodynamic blockage system

Inlet back pressuring through the aerodynamic blockage was performed using a high-pressure sonic nitrogen jet injected in the opposite direction to the isolator core flow at the exit plane. Nitrogen gas was issued from a high-pressure tank and was regulated to deliver the desired back pressure at the isolator exit. A solenoid valve with a flow coefficient ( $C_v$ ) of 3.3 controlled the issuing of the jet. The flow coefficient of the solenoid valve at high flow rate limit, which correspond to the present application, is defined as  $C_v = C \times (q[SLPM] \times \sqrt{T_1[K]})/(p_1[bar])$ , where  $q$  is the rated mass flow rate of the valve,  $C = 3273[bar/\sqrt{K}]$  is a dimensional constant and  $p_1$  and  $T_1$  are the air pressure and temperature upstream of the valve. The solenoid valve was actuated by a delay generator (Stanford Research Systems Inc., Model DG 645) that provided a pulse rise time defined as the time delay to reach the command voltage amplitude of within 1 ps. A stainless-steel tube of 5 mm (inner diameter) was connected to the solenoid valve and the other end of the tube was located 1.5 mm ( $\pm 0.5$  mm) downstream of the isolator exit plane and aligned to the isolator centre axis.

The characterization of the nitrogen jet was undertaken on a benchtop setting to quantify the strength and rise time of the jet. Compared with the set point jet total pressure, the actual jet total pressure was observed to be substantially lower because of the pressure head loss across the solenoid valve. Therefore, an independent quantification of the actual jet total pressure was made using the Mach disk standoff distance using schlieren imaging. A sample schlieren image of the jet at a set point total pressure of  $p_j = 2.74$  MPa issuing into ambient air is presented in figure 3. The measured ratio of the Mach disk stand-off to the jet diameter was mapped to the corresponding total pressure using the empirical relationship of Crist, Glass & Sherman (1966). The jet-to-isolator mass flow ratio estimates (isolator mass flow calculated at tare condition) are 2.6 %, 3.9 % and 5.2 % for  $p_j = 1.37$  MPa, 2.07 MPa and 2.74 MPa, respectively. The corresponding effective back pressure ratio  $p_b/p_\infty$  that the inlet/isolator is subject to were determined to be  $p_b/p_\infty = 6.8$ ,  $p_b/p_\infty = 8.0$  and  $p_b/p_\infty = 8.8$  for the jet injection pressures of  $p_j = 1.37$  MPa, 2.04 MPa and 2.74 MPa, respectively, as shown in § 3.4.

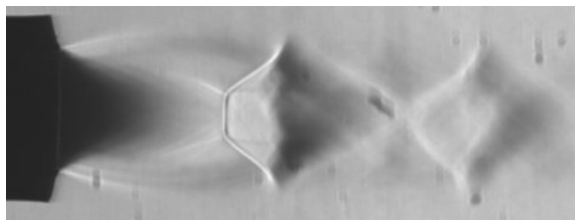


Figure 3. Schlieren imagery of the underexpanded nitrogen jet issuing into ambient air at a set point jet injection pressure of  $p_j = 2.74$  MPa. The Mach disk location was employed to calculate the observed stagnation pressure of the nitrogen jet.

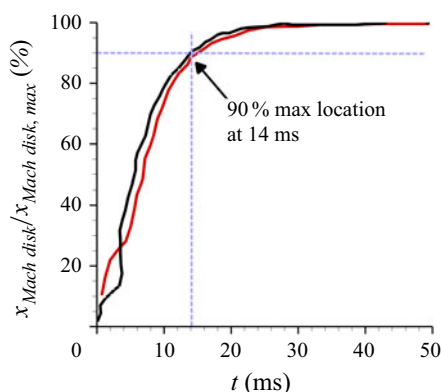


Figure 4. Time trace of the Mach disk distance from the jet exit as a percentage of its steady state distance for two different set point jet injection total pressures: (black)  $p_j = 1.37$  MPa and (red)  $p_j = 2.74$  MPa.

The rise time of the nitrogen jets was also quantified using high repetition rate schlieren imaging that imaged the progression of the jet from trigger start until when the Mach disk reached its equilibrium position. With this approach, the transient motion of the Mach disk while the jet mass flow increased to the set point value was tracked in a time resolved manner. Figure 4 presents the Mach disk distance from the jet exit as a function of time for two different jet injection total pressures  $p_j = 1.37$  MPa (black curve) and  $p_j = 2.74$  MPa (red curve);  $t = 0$  is defined as the frame where the Mach disk first appeared in the schlieren image. A moving time average filter was employed to smoothen the shot-to-shot variations in the location. It can be observed from figure 4 that the initial motion of the Mach disk was rapid until it reaches approximately 90 % of its final distance from the jet exit. Whereas it took  $t = 14$  ms for the Mach disk to reach its 90 % distance, it took until  $t = 30$  ms before the Mach disk reached its final location. Interestingly, this rise time was identical across all the back pressures that were implemented in this work. For the reported experiments, the jet was injected 2 s after a steady flow was established within the isolator and duration of a stable jet injection was 1.5 s; all the results presented in this work were obtained during this 1.5 s time window.

### 2.3.2. Physical blockage system

Inlet back pressure using physical blockage was performed by a right-circular cone with 38 mm base diameter, which was moved into the isolator from its exit plane centreline to reach the desired location corresponding to the set point back pressure. The cone



motion was actuated by a pneumatic system connected to a solenoid valve. The maximum speed of the cone blockage was approximately  $10 \text{ m s}^{-1}$  and it took approximately 50 ms from the trigger for the blockage to reach its set point location. The trigger signal to the blockage was given approximately 2 s after the start of wind tunnel run, by which time the steady state condition was obtained within the isolator. The blockage was left at the fully deployed state throughout the test run. From § 3.4 presented subsequently, the effective back pressure ratio provided by the fully deployed physical blockage was  $p_b/p_\infty = 10.0$ .

The test data collection started when the trigger to the pneumatic system was given, and the pressure field were collected over a duration of 2 s starting from the trigger signal. The dataset corresponding to the transient shock response during the cone actuation were truncated and approximately 1.5 s of pressure field dataset, when a steady back pressure ratio was obtained, was used for further processing. Therefore, the datasets are devoid of any influence from the time variations in back pressure. Furthermore, there were no measurable variations in the moving average isolator pressure fields when the average was taken over sufficiently long window to remove the shock oscillation transience. Therefore, there is abundant evidence that indeed a constant back pressure ratio was maintained while the shock train dynamics were probed.

## 2.4. Measurement methods

### 2.4.1. Surface streakline visualization

Surface streakline visualizations were performed to gain a qualitative exposure of the back-pressured isolator flow unit and estimate the separation length scale. The visualization medium consisted of mineral oil mixed with a dye pigment that fluoresced red when exposed to ultraviolet light, providing excellent contrast against the black model surfaces. The dye mixture was dragged by the wall shear, resulting in streakline patterns that qualitatively correspond to the local mean wall shear. In this way, regions of low shear stress (near the separation line, for instance) and shock feet could be identified through pigment accumulation. Moreover, as the pigment followed the flow over the entire duration of each test, the near wall streakline trajectories was used to deduce the dominant vortices within the isolator duct. Surface streakline videos were recorded at 60 Hz using a Nikon D5200 digital single-lens reflex camera, with illumination provided by a 10 W light-emitting-diode ultraviolet flashlamp. The streakline visualization images presented in the present work are averaged over 100 frames obtained during 1.5 s of steady wind tunnel operation. It should be noted that the objective of the surface streakline visualization was to capture the mean location of the leading shock of the shock train, the baseline isolator shock foot as well as other dominant features in occur in the back pressured situation. During the experiments, the oil would have typically stretch itself to a smooth film of thickness estimated to be of the order 0.01 mm. This thickness was substantially lower than the roughness height required to modulate the isolator boundary layers and the separated flow.

There were several practical challenges with obtaining crisp imagery in the present test article. The first set of challenges occurred because the visualization was performed in an internal flow geometry. The oil/pigment mixture was painted over an azimuthal-half of the duct extending along the duct length and the oil/pigment mixture was made to flow under wall shear. However, the starting shock through the duct invariably splashed the oil/pigment mixture and coated the viewing side of the duct. This caused some clouding of the viewing side during the imaging duration. Next, the back pressure was activated 2 s after steady isolator baseline flow was established to ensure that there are no extraneous effects from the transient back pressure while the isolator shock train set up. However, over

the 2 s duration, a substantial portion of the oil/pigment mixture was swept outside the measurement domain. Therefore, a considerably lesser amount of pigment was available to be imaged while the back pressure was activated; hence, the signal levels were smaller in the flow features downstream of the shock train, such as the separation vortex and reattachment loci. Furthermore, the region upstream of the leading shock of the shock train had a fixed (steady) flow pattern during back pressuring, and this resulted in a higher signal-to-noise ratio compared with the shock train region. In the latter, the surface streakline field continued to evolve over the imaging duration, and the averaging process integrated instances of high and low signals at a given pixel, which reduced the signal to noise ratio. Thirdly, it was difficult to homogenize the dye powder in the oil. This spatial inhomogeneity resulted in locations of higher and lower signals in the isolator baseline shock region which should have been uniform. Finally, the curvature of the axisymmetric isolator walls naturally caused lensing and blurring of images towards the top and bottom edges; this limited the visualization to  $-60^\circ \leq \phi \leq +60^\circ$ . During postprocessing, all the three camera channels were optimized to provide a balanced image that aids in visualizing all the major flow features.

#### 2.4.2. Pressure field imaging

High repetition rate 2-D pressure fields within the isolator are the primary datasets that will be used in this work. The pressure fields were imaged using high-speed polymer ceramic pressure-sensitive paints (PC-PSP). The paint composition followed the work of McMullen *et al.* (2013). A Ruthenium complex (Fisher Scientific catalogue number AA4412302) was chosen as the luminophore due its short luminescence lifetime of  $3\ \mu\text{s}$  as measured by Egami, Sato & Konishi (2019). The pressure/temperature sensitivities and luminescence intensity of the PC-PSP were also impacted by the selected binder components and composition. A binder particle weight fraction of 70 % was selected; the polymer and ceramic components were single component room temperature vulcanizing silicone rubber (Shin-Etsu Chemical) and hexagonal boron nitride nanoparticles (US-Nano Inc., catalogue number US2019), respectively. The particle weight fraction was selected as a compromise between response time, luminescence intensity and degradation rate. Room temperature vulcanizing polymer was selected for its superior response time and pressure sensitivity (Egami *et al.* 2019). Toluene was used as a solvent, giving the paint mixture a sprayable consistency. The resulting (approximate) properties of the PC-PSP are a pressure sensitivity of  $S_p = 0.62\ \% \text{ K}^{-1} \text{ Pa}$ , a temperature sensitivity of  $S_T = 1.05\ \% \text{ K}^{-1}$ , a degradation rate of  $-23.3\ \%/\text{h}$  and a response time of  $10\ \mu\text{s}$ . The binder, luminophore and solvent were mixed and then applied to the model in a single step. The thickness of the resulting PC-PSP coating was measured in an earlier work over a representative area ( $1.7\ \text{mm} \times 1.2\ \text{mm}$ ) using a 3-D laser confocal profilometer; the average paint thickness over the measurement area was  $h \approx 12\ \mu\text{m}$  (Jenquin, Johnson & Narayanaswamy 2023). Funderburk & Narayanaswamy (2019b) generated the Bode curve for this paint mixture over range of this paint thickness and estimated a  $-6\ \text{dB}$  attenuation frequency of  $3\ \text{kHz}$ . The paint was *in situ* calibrated using a mean pressure field acquired from a commercial pressure-sensitive paint (ISSI Inc., Model uniFIB) that possessed a high-pressure sensitivity.

The implementation of pressure field imaging involved spraying a uniform coat of the PC-PSP on the isolator inner surface, followed by illuminating the surface with a high-power ultraviolet light to excite the paint fluorescence. The paint fluoresced with a broadband emission centred at approximately  $600\ \text{nm}$ . A high-speed scientific complementary metal oxide semiconductor camera (Photron Inc., Model: SA-X2) fitted

with a Nikon f/1.2 50 mm lens and a 590 nm long-pass filter imaged the paint fluorescence at 8 kHz. Funderburk & Narayanaswamy (2019b) validated the resulting PC-PSP pressure data and the shock oscillation power spectra until 4 kHz using redundant pressure measurements from high-frequency pressure transducers. The pressure field was imaged over one half of the circumference ( $-90^\circ \leq \phi \leq 90^\circ$ ) and spanned  $5.25D$  in the streamwise direction of which usable data was obtained over  $-70^\circ \leq \phi \leq 70^\circ$  due to camera distortions along the edges. The streamwise extent of the usable imaging region extended between  $4.0 \leq x/D \leq 8.5$ .

The data reduction from the raw fluorescence images to pressure fields started with background subtraction of any residual scattering from the model. This was followed by normalization of the resultant images with a reference ‘wind off’ image that was obtained at 1 atm and 300 K without the wind tunnel flow. Two different redundant approaches were employed for calibration. First, the calibration was performed in a pressure-controlled chamber maintained at 300 K; this approach provided an excellent control on the set point pressures but could not account for the minor decrease ( $\approx 3$  K) in test article surface temperature during the test run. Second, the calibration was performed with the mean pressure fields over the same test article covering the same field of view obtained using a low bandwidth commercial pressure-sensitive paint (PSP). The differences in the calibration constants of the linear pressure mapping between the two approaches was 5 %. Finally, the calibrated pressure fields were binned  $3 \times 3$  pixels following Varigonda & Narayanaswamy (2021) and Funderburk & Narayanaswamy (2019b) to provide the best signal-to-noise ratio of the pressure fields without impacting the dynamic content of the pressure field. The resulting digital resolution of the pressure fields was 0.61 mm per binned pixel. For the statistical analyses presented in this article, the pressure time series consisting of 60 000 pressure fields spanning five highly repeatable test runs (12 000 time-correlated pressure fields per run) were utilized. For the mean and root-mean-square (r.m.s.) fields, entire 60 000 pressure fields were directly employed. For power spectral density (PSD) and two-point statistics computations, the desired quantities were obtained for each run, considering 12 000 time-correlated pressure fields, and subsequently ensemble-averaged over five runs.

The authors note that there were negligible effects of other extraneous effects like paint scouring by aerodynamic surface forces. This was ascertained by: (i) observing that the mean PSP signal corresponding to the first 0.2 s and last 0.2 s of data collection for a given run varied by less than 0.5 %; and (ii) the mean PSP signal across five successive runs obtained over a two-hour duration varied by less than 2 %. It should be remarked that a more recent work by Wood *et al.* (2023) and subsequent in-house tests studied the paint surface fracturing and scouring by impinging a high momentum pulsed sonic jet on a coupon coated with the PC-PSP, and reported no observable material damage of the paint coat even after 500 impingement instances. Finally, it should be noted that even if minor paint scouring had occurred, it will not impact the quantitative results presented in this work because: (i) the mean pressure calibration was performed for each run, which removes the error in mean pressure fields caused by scouring; and (ii) any loss in luminophore due to scouring will only improve the paint dynamic response (at the expense of degraded signal level) because the paint response time constant is proportional to the square of paint thickness.

## 2.5. Computational simulations

The RANS simulations were performed in addition to the experiments to obtain qualitative information of the isolator shock train structure and an estimate of the effective average

back pressure that was imposed by the jet and cone injection approaches described above. Two-dimensional simulations corresponding to the isolator centre plane were performed using a commercial software, ANSYS FLUENT, and employed the in-built  $k - \omega$  shear stress transport turbulence model to handle the viscous flow that develop within the duct. The simulations also employed the symmetry condition about the duct centreline, and as a result, the flow field that developed within one half of the duct was computed. An unstructured mesh was created that had 47 344 grid points with adaptive grid spacing that is more clustered in the near wall region of the isolator duct. The nearest wall normal grid was located at  $4.5 \times 10^{-6}$  m, which corresponds to  $y/\delta \approx 0.75 \times 10^{-3}$  and a  $y^+ \approx 5$ , based on the boundary layer profile reported at  $x/D = 6.33$  by Leonard & Narayanaswamy (2021). The computations were performed with a uniform pressure boundary condition at the isolator exit. The exit pressure condition that matched the experimental leading shock foot location is reported as the effective back pressure for a given jet or cone injection setting.

### 3. Results and discussions

The flow field behaviour of the inlet/isolator without the application of back pressure (tare condition) is described first, and is followed by the inlet/isolator with back pressure application. For the discussions of back pressured inlet/isolator, the effective back pressure ratio will be used as the metric to describe the flow field response across both the jet injection and physical blockage configurations. The ensuing discussions will evidence that changing between jet and cone injection does not cause any extraneous features in the shock train dynamics that are generated by the injection approach.

#### 3.1. Baseline flow field characterization

The baseline flow field characterization was made at tare conditions (without back pressure) using a combination of planar laser scattering (PLS) for off-surface shock train imaging and surface pressure field. Over five test runs at the set point conditions were conducted and the baseline flow field for each run were highly repeatable with one another and with those of Leonard & Narayanaswamy (2021). Figure 5 shows the off-body shock train, visualized using PLS imaging, overlaid on the mean surface pressure field (figure 5a) and r.m.s. surface pressure field along the isolator (figure 5b) at tare condition. The shock waves that were discerned from the PLS images are annotated as dashed lines in both figures. An excellent agreement was observed between the shock foot locations obtained by interpolating the PLS images and from the mean and r.m.s. surface pressure fields. The off-surface shock train also evidences a modest shock angle, which suggests that the shock legs are too weak to cause any flow separation at tare condition. This suggestion is corroborated by the mean pressure jump across the shock foot at  $x/D = 7$ , which is substantially lower than the empirical estimate of the pressure jump required for flow separation. Furthermore, the  $p_{rms}$  field evidences an absence of flow separation at  $x/D = 7$  and other shock intersection locations between  $x/D = 4.1$ –8.5. Overall, the isolator did not exhibit any inherent shock induced separation at tare conditions that may further complicate the analysis of the back pressure configurations.

Both the mean and r.m.s. pressure fields, presented in figures 5(c) and 5(d), respectively, exhibit notable azimuthal uniformity. Examining the shock foot locations reveals a slight curvature that is symmetric about the centre azimuth; the end-to-end variation in the streamwise location of the shock foot across the azimuthal direction is  $0.02D$ . There is also a slight inflation ( $< 10\%$ ) in the mean pressure along  $\phi = 0^\circ$  compared with off-centre azimuths. Interestingly, the  $p_{rms}/p_w$  at the  $\phi = 0^\circ$  is slightly lower than the off-centre

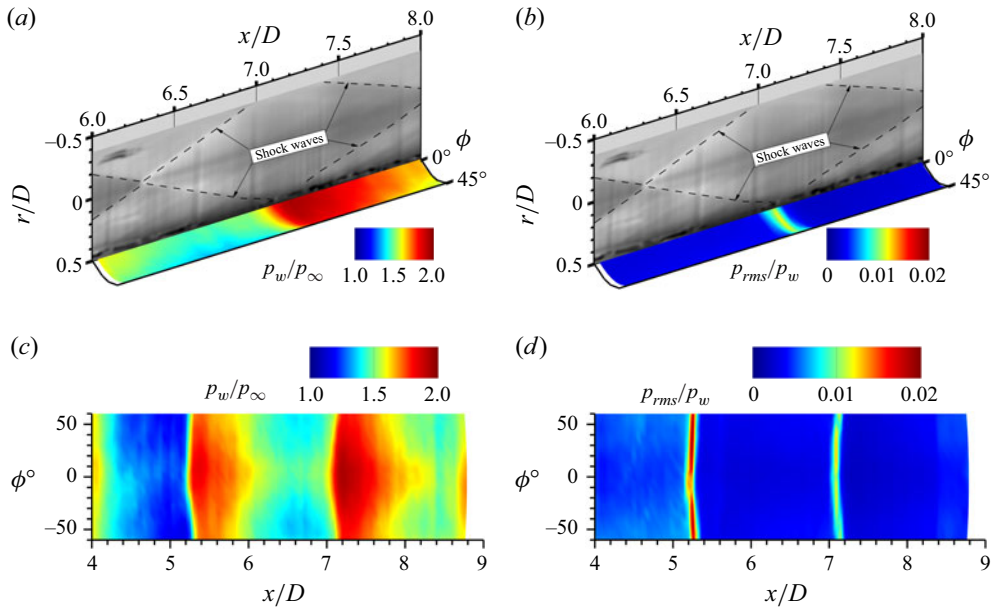


Figure 5. Characterization of the surface and off-surface flow field quantification of the isolator at tare condition. (a) Overlay of the mean surface and (b) r.m.s. pressure fields, respectively, and the corresponding off-surface shock structure visualization using planar scattering. Panel (c) presents the mean surface and panel (d) the r.m.s. pressure fields, respectively.

azimuths; the overall end-to-end variation in  $p_{rms}/p_w$  at a shock foot location is less than 10 % of the peak value. It is likely that these slight variations are caused by a combination of fluorescence light refraction through the curved walls of the isolator, slight image defocusing along the off-centre azimuths and residual image distortions that were left uncorrected from data processing. Another possibility for the azimuthal variation could also be the non-uniformity in the ultraviolet illumination due to the light focusing effects through the curved isolator wall which could cause higher intensity along  $\phi = 0^\circ$  and a lower intensity away from the centre azimuth.

### 3.2. Surface streakline imagery of back pressured isolator

Surface streakline imagery is first presented for the back pressured isolator to obtain a grasp of the global flow field structure within the isolator. The surface streakline imagery is particularly suited to visualize the shock foot, separation and reattachment loci, and dominant vortices that may be present within the flow unit. The surface streakline field for a jet total pressure of  $p_j = 1.75$  MPa is presented in figure 6. Examining the field along the downstream direction first reveals two shock foot at  $x/D \approx 5.2$  and  $x/D \approx 7.1$ , respectively, which correspond to the isolator baseline shock system. Interestingly, the location of these shocks remains unaltered compared with the tare case, which shows that the information about the presence of shock train has not propagated into the baseline shocks. Downstream of the isolator baseline shocks is the leading shock of the shock train. The footprint of this leading shock appears broader than the isolator baseline shocks due to the large amplitude unsteady motions executed by this shock. The boundary layer separates downstream of the leading shock, as evidenced by the accumulation of the pigment. The separated flow is observed to be dominated by the presence of a counter-rotating vortex pair (CVP) (see figure 6). These CVPs are likely the main source of fluid exchange



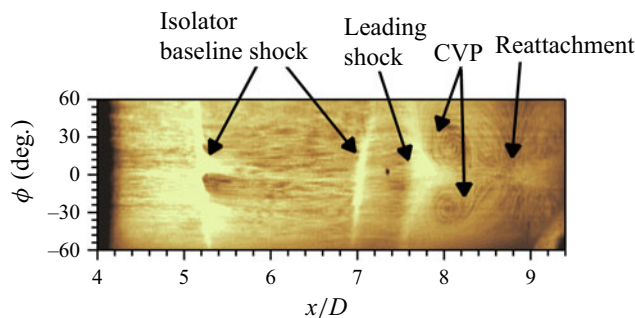


Figure 6. Surface streakline visualization showing the flow structure during back pressured operation.

between the viscous region and the core flow. The downstream edge of the CVPs marks the reattachment location, where convergence of the streakline traces is observed. No other major feature is discerned downstream of the reattachment locus. Interestingly, no imprints of the succeeding (trailing) shocks of the shock train are present in the streakline imagery. Two likely reasons for the absence of their footprints are that the succeeding shock foot are located farther downstream of the measurement domain for the pressure setting used in figure 6 and/or their footprint is masked by the thick viscous flows beneath the trailing shocks. It should be noted that the trailing shock feet become visible in the r.m.s. pressure field at elevated back pressures and are discussed in the subsequent sections. A spanwise average location of the separation and the reattachment were obtained and the corresponding separation length,  $L_{sep}$ , was determined to be approximately 38 mm (or  $\approx 1.0 D$ ) for figure 6. The estimated  $L_{sep}$  will be compared with other estimates made using the peak Strouhal number of wall pressure fluctuation power spectra in § 3.5.

### 3.3. Mean and r.m.s. pressure fields of back pressured isolator

The ensemble mean pressure fields of the back pressured isolator over different back pressure settings are presented in figure 7. A sharp increase in the mean pressure caused by the shock train within the isolator can be observed across all the back pressure settings. The location of this increase corresponds to the leading shock of the shock train (henceforth termed simply as ‘leading shock’). For the  $p_b/p_\infty = 6.8$  case considered in figure 7(a), the leading shock is located at  $x/D = 7.6$ , which is downstream of the two baseline shocks located within the measurement region. For  $p_b/p_\infty = 8.0$  presented in figure 7(b), the leading shock is located at  $x/D = 6.0$ , which is upstream of the baseline shock foot at  $x/D = 7.1$  and considerably downstream of the baseline shock foot at  $x/D = 5.2$ . For  $p_b/p_\infty = 8.8$  considered in figure 7(c), the leading shock foot is located at  $x/D = 5.1$ . For the  $p_b/p_\infty = 10.0$  (cone injection) case shown in figure 7(d), the leading shock is upstream of the measurement region. This is observed by noting that the surface pressure even at the most upstream location substantially exceeded  $p_w/p_\infty \approx 2.5$  that are observed just upstream of the shock train in figure 7(a–c). It is important to note that even the highest back pressure setting (figure 7d) did not unstart the inlet, i.e. the isolator shock train was not disgorged from the inlet. This can be discerned from noting that the pressure ratio  $p_w/p_\infty$  at the start of the measurement domain ( $x/D = 4.0$ ) is approximately 5.0. This  $p_w/p_\infty \approx 5.0$  can be observed to occur within one isolator diameter from the beginning of the shock train for  $p_b/p_\infty \leq 8.0$  and  $p_b/p_\infty \leq 8.8$  shown in figure 7(b,c). In fact, a more precise estimation of the leading shock location was obtained to be  $x/D = 3.75$  in the following paragraphs.



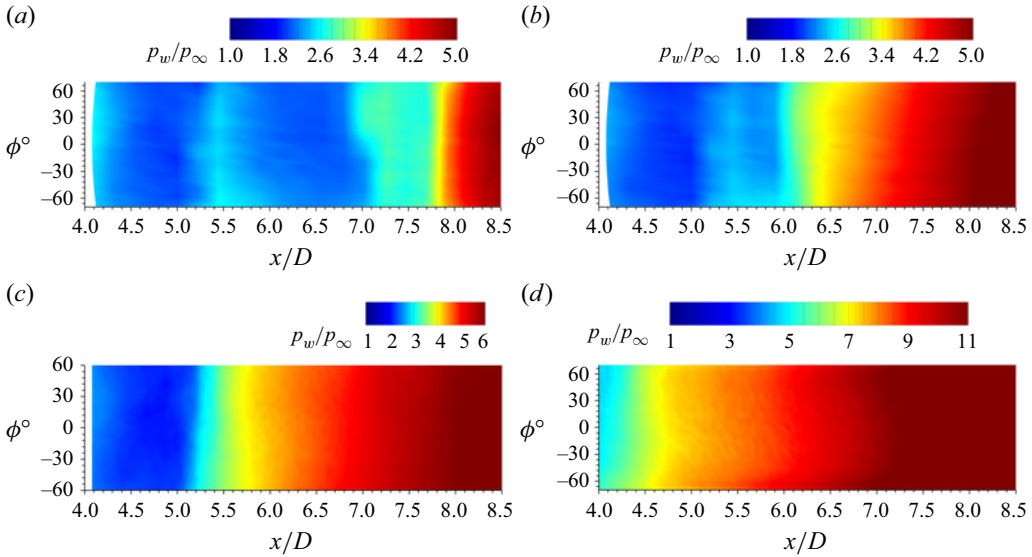


Figure 7. Mean surface pressure field within the isolator at different back pressure setting: (a)  $p_b/p_\infty = 6.8$ ; (b)  $p_b/p_\infty = 8.0$ ; (c)  $p_b/p_\infty = 8.8$ ; (d)  $p_b/p_\infty = 10.0$  (cone injection).

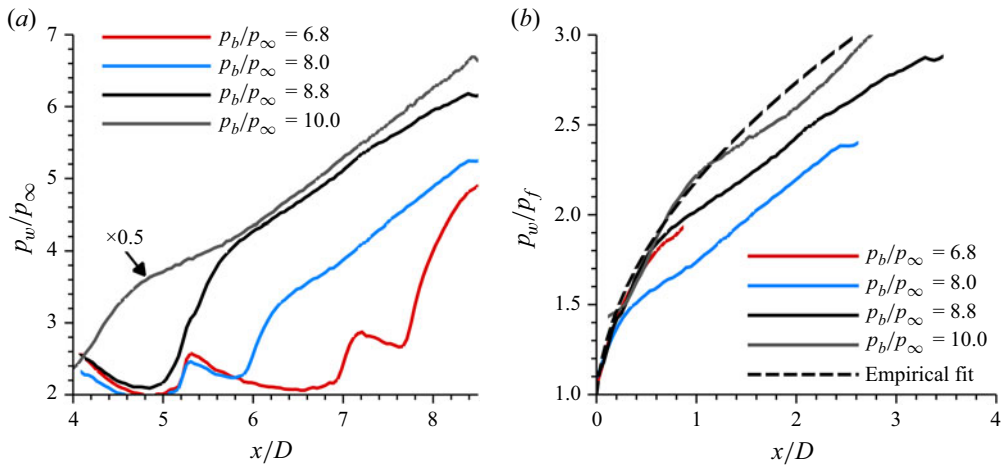


Figure 8. Mean centreline surface pressure field within the isolator at different back pressure settings: (a) surface pressure along the entire isolator normalized by free stream, and (b) surface pressure only within the pseudoshock region normalized by pressure just upstream of the pseudoshock.

The mean pressure profiles along the isolator length measured at  $\phi = 0^\circ$  for different back pressures are presented in figure 8. The profiles along the entire length of the isolator are provided in figure 8(a) and the profiles are normalized by the free stream pressure upstream of the inlet. Furthermore, the pressure profiles with  $p_b/p_\infty = 10.0$  (cone injection) was scaled by half to make the values comparable to the other profiles. The pressure profiles presented in figure 8(b) were normalized by the corresponding mean pressure just upstream of the leading shock ( $p_f$ ); no scaling was made on  $p_b/p_\infty = 10.0$  (cone injection) case. The  $x = 0$  in figure 8(b) starts at the leading shock of the shock train and ends where the field of view terminates. For example, the back pressure  $p_b/p_\infty = 6.8$

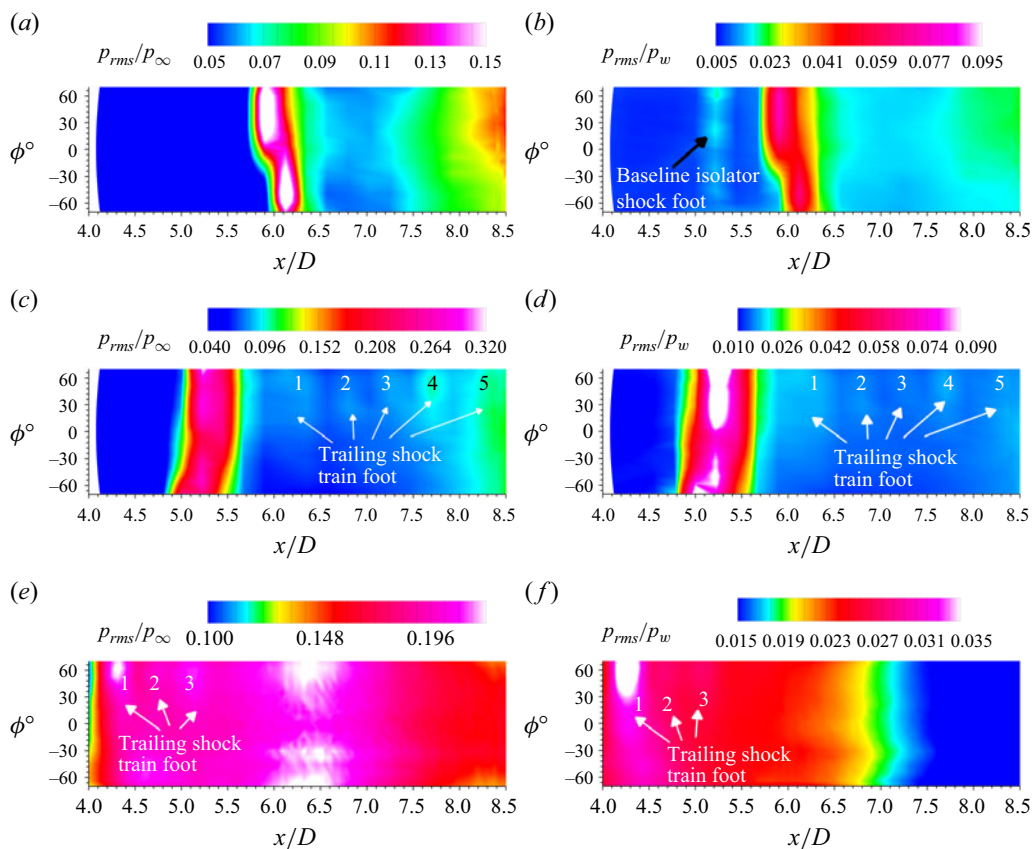


Figure 9. The r.m.s. surface pressure field within the isolator setting at different back pressure settings: (a,b)  $p_b/p_\infty = 8.0$ ; (c,d)  $p_b/p_\infty = 8.8$ ; (e,f)  $p_b/p_\infty = 10.0$ . The r.m.s. fields were normalized by the free stream pressure upstream of the inlet in (a), (c) and (e), and by the local mean surface pressure in (b), (d) and (f).

has the leading shock at  $x/D = 7.5$  while that for  $p_b/p_\infty = 8.0$  and  $p_b/p_\infty = 8.8$  occurs at  $x/D = 6.1$  and  $x/D = 5.1$ , respectively. However, the pressure fields for all cases terminate at  $x/D = 8.7$ . As a result,  $p_b/p_\infty = 6.8$  case has a much less measured extent downstream of the leading shock and seems incomplete. With this input, it is observed from figures 8(a) and 8(b) that all the profiles within the shock train exhibit an initial steep increase in the mean pressure over the first  $0.4D$  that is followed by a more gradual increase farther downstream. Comparing the streamwise extent of the initial increase and the  $p_{rms}$  field shown in figure 9, it is observed that this initial pressure rise region coincides with the intermittent region over which the leading shock oscillates. This confirms that the initial pressure rise is indeed caused by the leading shock, which is also consistent with the past observations (e.g. Carroll *et al.* 1993). It can be also observed in figure 8(a) that the slope of the initial pressure rise is very similar across the different back pressures, which portrays similar leading shock strengths across different back pressure settings. This again is consistent with the literature on back pressured supersonic ducts (Hunt & Gamba 2018) that examined the pressure fields over different back pressures. Furthermore, the pressure jump across the leading shock is determined to be sufficient to cause shock induced separation for all back pressure settings presented, based on the empirical correlations (Babinsky & Harvey 2011). The gradual pressure rise downstream of the first  $0.4D$  corresponds to the separated flow generated by the leading shock. Unlike Hunt & Gamba

(2019) who noticed undulation in the mean pressure field from the trailing shocks of the shock train, such undulations are not observed in this work; however, the trailing shock footprints are observed in the  $p_{rms}$  fields that will be presented subsequently.

A comparison of the measured pressure profiles was made with the empirical profile of Waltrup & Billig (1973). The measured boundary layer thicknesses at  $x/D = 6.33$  were used for the inflow parameters required for this profile. Furthermore, the approach Mach number was computed based on the measured static pressure ratio just upstream of the leading shock foot of the shock train and the free stream pressure. Given the modest dependence of the empirical profile on the inflow boundary layer properties, the approximations made towards computing the boundary layer thickness are expected to minimally impact the pressure trends. Figure 8(b) presents the empirical pressure profile as a dashed curve. The profiles of the  $p_b/p_\infty = 10.0$  (cone injection) case were shifted in  $x$  direction until an agreement was obtained with other profiles. It can be observed that the initial pressure rise until  $x/D \approx 0.4$  is similar between the empirical and experimental pressure profiles across the different back pressure settings. A stronger deviation in the experimental and empirical profiles occurs at more downstream locations, wherein the empirical profile overpredicts the pressure values compared with the experiments. Overall, the best agreement between the empirical and experimental profiles occurs with  $p_b/p_\infty = 10.0$  (cone injection) case, while  $p_b/p_\infty \leq 8.8$  cases exhibit noticeable departures, especially for  $x/D > 0.4$ . Between the different back pressures, whereas the pressure profiles with  $p_b/p_\infty = 10.0$ ,  $p_b/p_\infty = 8.8$  and  $p_b/p_\infty = 6.8$  exhibit a nearly identical evolution over  $x/D \leq 0.6$ , the profile with back pressure  $p_b/p_\infty = 8.0$  exhibits a departure to a lower value for  $x/D > 0.3$ . While the reason for this departure is not clear, we posit that the leading shock foot and the initial part of shock train possibly interacts with the expansion fan emanated within the isolator from the upstream undisturbed flow at this back pressure setting. This is observed from the mean pressure profile of figure 8(a) where the leading shock with  $p_b/p_\infty = 8.0$  is located in the region of pressure decrease (expansion region), contrasting the other back pressures where the leading shock is located near zero pressure slope. It can also be observed from figure 8(b) that the first data point within the measurement location for  $p_b/p_\infty = 10.0$  (cone injection) occurs at  $x/D = 0.25$ ; this places the location of the leading shock for the  $p_b/p_\infty = 10.0$  case at  $x/D = 3.75$ .

Figure 9 presents the r.m.s. pressure fields within the isolator section for two different jet injection cases,  $p_b/p_\infty = 8.0$  (figure 9a,b),  $p_b/p_\infty = 8.8$  (figure 9c,d) and  $p_b/p_\infty = 10.0$  (figure 9e,f). Whereas the r.m.s. fields of figure 9(a,c,e) are normalized by the free stream pressure, the r.m.s. fields of figure 9(b,d,f) are normalized by the local mean surface pressure. Moving along the isolator length for  $p_b/p_\infty \leq 8.8$ , the initial regions of the isolator upstream of the shock train exhibit a uniform  $p_{rms}/p_\infty$  field. Minor elevations are observed corresponding to the baseline isolator shock that were not perturbed by the shock train; however, these undulations ( $\approx 0.02$ ) are not visible with the present colourmap settings. A strong increase in the  $p_{rms}/p_\infty$  can be observed beneath the leading shock foot and the  $p_{rms}/p_\infty$  reaches its maximum value along the isolator length beneath the leading shock foot. The  $p_{rms}/p_\infty$  subsequently decreases to a relative plateau (observed as a near uniform contour colour between  $x/D \approx 6.6 - 7.3$  in figure 9a, for example) and is followed by a gradual increase in the downstream regions. Multiple minor peaks in the  $p_{rms}/p_\infty$  can be identified with  $p_b/p_\infty = 8.8$  in figure 9(c) that correspond to the trailing shock feet. These peaks are diffuse due to the presence of thick viscous layer beneath the shock foot that dissipates the shock into weak compression waves. Interestingly, the strengths of the individual peak  $p_{rms}/p_\infty$  are different from one another. Whereas  $p_{rms}/p_\infty$  local peak exhibits a decreasing trend between the shocks labelled '1' to '3', subsequent shock legs '3' to '5' exhibit an increasing trend. The relative strength of the

$p_{rms}$  with respect to the local mean pressure (shown in [figure 9d](#)) also exhibits this trend and reiterates a weakening and strengthening of the shock feet unsteadiness within the shock train. The trailing shock train feet are not clearly defined with  $p_b/p_\infty = 8.0$  and  $p_b/p_\infty = 6.8$  (not presented). However, a broad increase in  $p_{rms}/p_\infty$  was observed with a modest peak at  $x/D \approx 8$  for  $p_b/p_\infty = 8.0$  (see [figure 9a,b](#)).

The  $p_b/p_\infty = 10.0$  (cone injection) case in [figure 9\(e,f\)](#) reveal an overall elevation in the  $p_{rms}/p_\infty$  and a appreciably similar  $p_{rms}/p_w$  values within the shock train when compared with the  $p_b/p_\infty = 8.8$  case. Similar to the  $p_b/p_\infty = 8.8$  case, [figure 9\(e,f\)](#) reveal the presence of three identifiable trailing shock feet. These shock feet are notably closer to one another for compared with  $p_b/p_\infty = 8.8$  of [figure 9\(c,d\)](#). An extensive region of the flow downstream of the shock train is devoid of any noticeable shock foot and this region likely corresponds to the subsonic mixing process of the pseudoshock (more confirmation in § 3.4). Finally, the  $p_{rms}/p_\infty$  fields show noticeable variations across the azimuthal direction. The variations are especially stark in the trailing edge shock feet; whereas the trailing edge shock feet is clearly delineated for  $\phi > 0^\circ$ , the imprints of the shock feet are not visible for  $\phi < -30^\circ$ . To elaborate on a few possible causes of this asymmetry, it should be noted that the basic architecture of the wind tunnel converging–diverging nozzle has its curvature occur only along the top wall, while the bottom wall is straight. This differential curvature may cause the boundary layer thickness be different from the top and bottom walls, which in turn may cause a different mass displacement from the top and bottom walls. This in turn can cause the inflow to the inlet to have a very small angle. This minor flow incidence angle did not impact the isolator baseline flow symmetry to a measurable level. When the shock waves continued to process the inlet flow, the asymmetry possibly got amplified with increasing distance within the isolator. This can be seen in [figure 5\(d\)](#) when one compares the baseline shock at  $x/D = 5.2$  and  $8.7$ . When the back pressuring jet is fed by this mildly asymmetric flow, the resulting shock train further possibly amplifies the asymmetry to measurable levels. This asymmetry also compounded by the differential illumination of the PSP and other secondary effects.

It should be reiterated that the isolator duct of the present work cannot be considered narrow. The narrowness is determined by  $\delta^*/D$ , which is 0.048 for the present isolator duct at a location just upstream of the leading-edge shock (see [figure 2](#)). This means that the displacement effect of the viscous region is felt only within 10 % of the flow ( $2\delta^*/D$  overall). Therefore, the upstream shock is interacting with a rather thin boundary layer compared with the duct height. In fact, the RANS simulations, presented subsequently, show that a substantial portions of the individual shocks (leading and trailing) of the shock train are straight, which suggests that a major portion of the isolator flow within the shock train can be considered as inviscid. The natural development of shock train culminates with a viscous mixing region that engulfs the entire duct. This is true for all isolator cross-sections and blockage ratios, narrow and broad; for narrow ducts, this region occurs earlier along the isolator length. For the present study, the mixing region occurs only for  $p_b/p_\infty \geq 8.8$ , which again reiterates that the duct may not be considered narrow. Finally, we also note that the pressure rise curve matches remarkably well with the empirical fit of Waltrup & Billig (1973) ([figure 8b](#)) that were based on experimental datasets obtained in a relatively low blockage duct. This is yet another proof that the present isolator duct upstream of the shock train is not viscous flow dominated.

### 3.4. Estimated effective back pressure and shock train structure

The streamwise locations of the leading shock foot from the mean and r.m.s. pressure fields were used to map the effective back pressures by comparing the corresponding shock

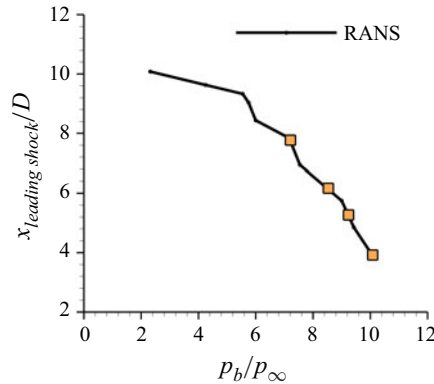


Figure 10. Computed leading shock foot location at different back pressures (black dot curve) and the experimental leading shock foot location overlaid on the plot to estimate the effective back pressures for different injection settings.

train leading-edge locations of RANS simulations. This effective back pressure should be differentiated from the pressure downstream of the shock train that is measured and presented in figure 7. The effective back pressure provided in this section represents a uniform exit (back) pressure of the duct that generates the leading shock at the measured location for the given inflow Mach number and a given blockage. Figure 10 presents the variation of the leading shock foot location ( $x_{\text{leading shock}}$ ) at various uniform back pressures imposed at the isolator exit in RANS simulations. Square symbols were added in the plot to identify the leading shock foot locations at different jet and cone injection settings and obtain an estimate of the corresponding effective back pressures. The RANS simulations show that a minimum back pressure of  $p_b/p_\infty \approx 2.0$  is needed to set the shock train within the isolator. The leading shock foot location moves upstream rather modestly for  $p_b/p_\infty < 5.0$  and exhibits a much stronger upstream movement for higher back pressures. Juxtaposing the experimental leading shock location of the shock train with the simulated values estimates the back pressure ratios at  $p_b/p_\infty \approx 6.8$  (for  $p_j = 1.37$  MPa),  $p_b/p_\infty \approx 8.0$  ( $p_j = 2.04$  MPa),  $p_b/p_\infty \approx 8.8$  ( $p_j = 2.74$  MPa) and  $p_b/p_\infty \approx 10.0$  (for cone injection).

The isolator shock train structure is investigated using the velocity divergence fields at the duct centre plane from the RANS simulations at different set point effective back pressures that nearly correspond to the respective jet injection and cone injection settings. A qualitative representation of the divergence fields for various set point conditions are presented in figure 11(a–d). The leading shock of the shock train are labelled in all the figures. It can be observed that the isolator duct is interwoven by the baseline shock train, whose intersection locations with the isolator surface make a good comparison with the figure 5(d). Consistent with the experiments, baseline shocks are very weak and do not exhibit any boundary layer separation.

The shock train from back pressure application also exhibits agreement in the spacing between the leading shock and the successive trailing shocks. Further, the diffusion of the trailing shock near the isolator surface can also be observed across all of figure 11(a–d), which caused the smearing of the pressure gradient observed in the  $p_{rms}/p_w$  fields. The shock trains also show interesting similarities and differences between one another with increasing back pressure. The leading and trailing shocks across all set points exhibit a short region around  $r/D = 0$  where they are normal and they become oblique away from  $r/D = 0$ . The boundary layer downstream of the leading shock is separated for all



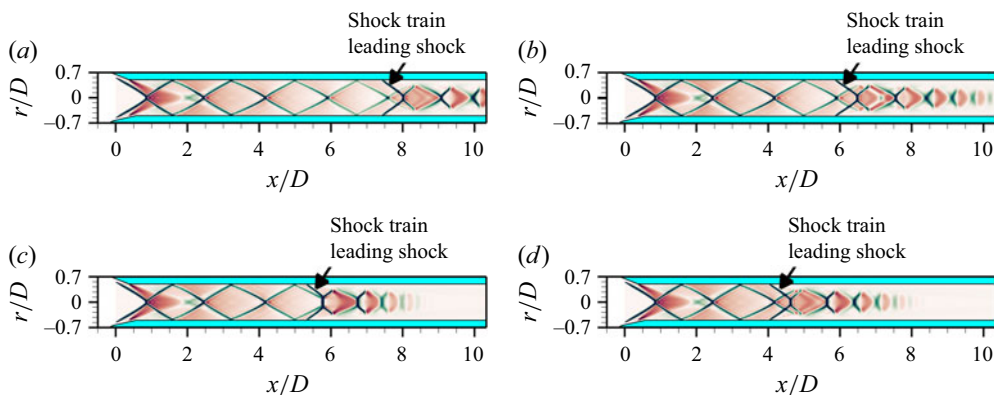


Figure 11. Computed velocity divergence field from RANS simulations at different back pressure settings that approximately corresponds to (a)  $p_b/p_\infty = 6.8$ , (b)  $p_b/p_\infty = 8.0$ , (c)  $p_b/p_\infty = 8.8$  and (d)  $p_b/p_\infty = 10.0$ .

back pressures presented, and thick viscous regions where the shock is dissipated can be observed near the isolator surface extending along the entire downstream duct length. Interestingly, while the trailing shocks can be traced until the isolator exit in figure 11(a,b) that correspond to  $p_b/p_\infty = 6.8$  and  $p_b/p_\infty = 8.0$ , the trailing shock is dissipated into the viscous mixing region in figure 11(c,d) that correspond to  $p_b/p_\infty = 8.8$  and  $p_b/p_\infty = 10.0$ , respectively. Even between figures 11(c) and 11(d), figure 11(d) exhibits a noticeably larger streamwise extent of the mixing region.

### 3.5. Wall pressure PSD

The frequency content of the wall pressure fluctuations at different locations upstream and within the shock train are presented next. The PSD was computed for each data set that spanned 1.5 s of run time (12 000 data samples per run) using Welch's algorithm with a 512 sample for each block. A Hanning window with 50 % overlap was employed while computing the PSD. This resulted in a frequency resolution  $\Delta f = 7.8$  Hz which is sufficient to delineate the PSD across the entire canonical shock wave boundary layer interactions (SBLI) with acceptable noise within the PSD.

As a baseline, the pressure fluctuation PSD for the isolator without back pressure is first presented. Figure 12 shows the frequency premultiplied PSD beneath the shock foot of the baseline (tare) isolator located at  $x/D = 5.2$ ; the PSD was averaged over  $-30^\circ \leq \phi \leq +30^\circ$ . Figure 12 also presents the corresponding frequency premultiplied PSD of the incoming boundary layer averaged over  $4.2 \leq x/D \leq 4.7$  and  $-30^\circ \leq \phi \leq +30^\circ$ . The premultiplied PSD is a standard practice to show the relative contribution of the PSDs spanning several decades of frequency. The linear y-scale is the best representation to visualize the relative contributions and has been extensively used in the SBLI literature. The PSD beneath the boundary layer shows a monotonically increasing trend over the entire measured frequency range. This PSD trend is expected since the peak energy of the upstream boundary layer occurs at the characteristic boundary layer frequency ( $u_\infty/\delta$ ) that is over an order of magnitude higher than the Nyquist frequency.

The frequency premultiplied PSD beneath the isolator shock foot shows a broadband spectrum with a modest peak at a very low frequency  $f \approx 70$  Hz. This peak is followed by a slight minimum at  $f \approx 120$  Hz and a subsequent monotonic increase. Despite there not being a shock-induced flow separation, the isolator shock foot exhibits low frequency pulsations; the cause for these pulsations has to do with the dampening of the shock foot



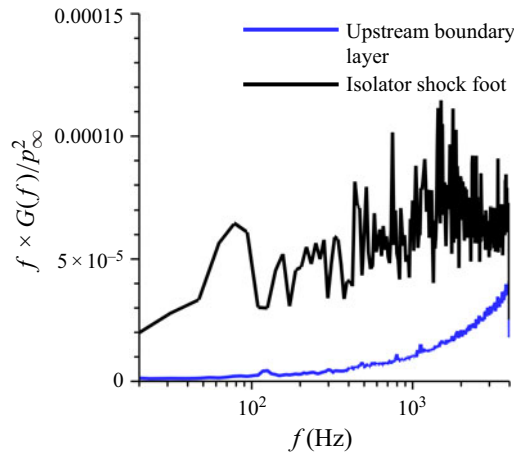


Figure 12. The PSD of the isolator surface pressure fluctuation beneath the shock foot (black) and the upstream boundary layer (blue) for the tare configuration.

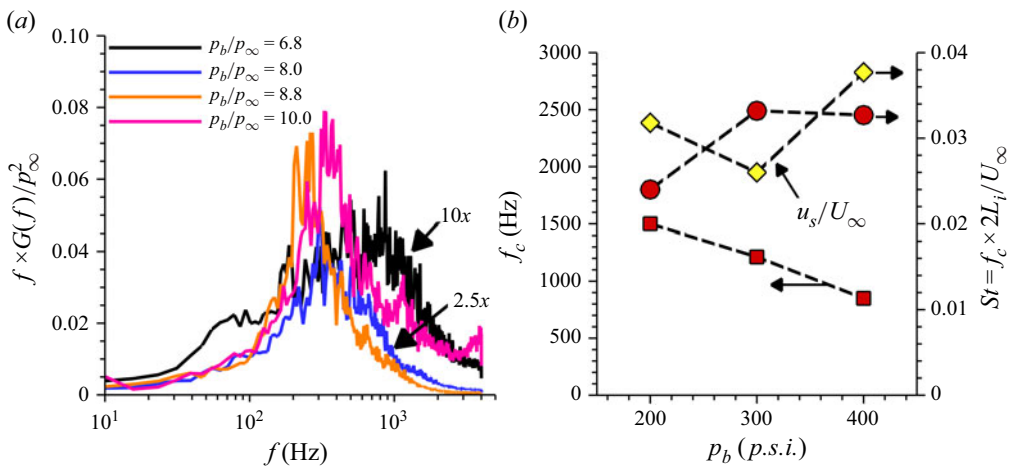


Figure 13. (a) The PSD of the leading shock intermittent region surface pressure fluctuations for the different back pressure settings, and (b) evolution of the leading shock foot zero crossing frequency, velocity and Strouhal number based on these parameters across different jet injection pressures. The horizontal arrows point to which y-axis the given plot will correspond to.

jitter due to the boundary layer turbulent structures passage by viscous forces (detailed in Leonard & Narayanaswamy 2021). Finally, it should be noted that the PSD amplitude beneath the different shock feet along the isolator section are within the same order of magnitude as the boundary layer PSD. Overall, the unsteady shock oscillations are observed to be quite weak without the application of back pressure.

The corresponding frequency premultiplied PSD beneath the leading shock is presented in figure 13(a) for different back pressure settings; the PSDs are appropriately scaled to make suitable comparisons. It can be observed that the PSDs for all back pressure settings exhibit broadband aperiodic motions with a broad peak at its most dominant frequency. This peak frequency decreases with increasing back pressure from approximately 800 Hz at  $p_b/p_\infty = 6.8$  to 240 Hz at  $p_b/p_\infty = 8.8$ ; concomitantly the frequency spread of the

PSD also decreases by over a decade between  $p_b/p_\infty = 6.8$  and  $p_b/p_\infty = 8.8$ . The magnitude of the PSD increases by over a factor of 10 by increasing the back pressure from  $p_b/p_\infty = 6.8$  to  $p_b/p_\infty = 8.8$ .

Figure 13(a) also presents the pressure fluctuation PSD at the most upstream measurement location for  $p_b/p_\infty = 10.0$  ( $x/D = 4.0$ ); readers are reminded that the leading shock for this setting is upstream of the measurement domain. It will be shown from the subsequent discussions that the intermittent region of the leading shock extends over  $0.5D$  for  $p_b/p_\infty = 8.8$ , which is expected to hold for  $p_b/p_\infty = 10.0$  as well, given the close similarity of  $p_b/p_\infty$  values. Therefore, the location  $x/D = 4.0$  where the PSD is presented in figure 13(a) is  $x/D \approx 0.25$  downstream of the pseudoshock leading edge, which is within the leading shock intermittent region. The PSD with  $p_b/p_\infty = 10.0$  also exhibits a broadband spectrum with a peak in PSD that occurs at approximately 300 Hz. The near constancy of the peak PSD frequency observed with increasing back pressure between  $p_b/p_\infty = 8.0$  and  $p_b/p_\infty = 10.0$  is also consistent with a similar observation of the near constant shock stem oscillation frequency with increasing back pressure made by Hunt & Gamba (2019). It should be noted that the strength of the PSD for  $p_b/p_\infty = 10.0$  is very similar to  $p_b/p_\infty = 8.8$ . However, since the location where the PSD was obtained for  $p_b/p_\infty = 10.0$  is situated downstream of the peak  $p_{rms}$  location, it is expected that the PSD beneath the shock foot for  $p_b/p_\infty = 10.0$  will exceed  $p_b/p_\infty = 8.8$ , which continues the increasing trend of the PSD with back pressure.

The broadband aperiodic nature of the leading shock oscillations has been observed in other works with supersonic isolators (Xiong *et al.* 2017; Hunt & Gamba 2019). The question is if the leading shock foot motions adhere to SBLI, given the significant complexities that occur downstream of the leading shock. This question is addressed first by examining the features of the separation shock dynamics and subsequently using cross-correlation analysis. Prior works on canonical SBLI had successfully scaled the shock oscillation frequency and shock velocity using the shock zero crossing frequency and the intermittent region length defined as the distance between 5 % to 95 % of the shock foot oscillation amplitude; these measurements were made in the prior works using pointwise measurements at a relatively coarse resolution. The 2-D pressure fields of the present study provide a much finer spatial resolution that enables a closer examination of the Strouhal number scaling and an independent examination of the leading shock foot speeds at different back pressure settings. Figure 13(b) presents the shock zero crossing frequency ( $f_c$ ) measured at the peak  $p_{rms}$  location at different back pressure settings. The  $f_c$  exhibits a monotonic decrease with increasing back pressure with an overall decrease of 50 % between  $p_b/p_\infty = 6.8$  and  $p_b/p_\infty = 8.8$ . It is interesting to note that the magnitude of  $f_c$  is between a factor of two to three higher than the peak frequency of the frequency premultiplied PSD of the pressure fluctuation presented in figure 13(a). The Strouhal number based on  $f_c$  and the intermittent length  $L_i$  (region over which the intermittency factor lie between 0.05 and 0.95), presented in figure 13(b), exhibits a remarkably tight agreement in their values across the different back pressures spanning a range between 0.026 to 0.033. These values are also in excellent agreement with the Strouhal number (based on separation scale) range of the separation shock oscillations in canonical SBLI, which are reported to occur between 0.02–0.05 (Gonzalez & Dolling 1993; Dussauge & Piponniau 2008). Clemens & Narayanaswamy (2014) argue that the Strouhal number can also be viewed as the ratio of the separation shock speed to the free stream velocity. While their argument used an estimated shock speed as  $2L_i \times f_c$ , the present study allows an independent determination of the shock speed by tracking the leading shock foot motions from the pressure fields. The instantaneous location of the leading shock foot was taken where the local pressure exceeds the inflow static pressure by 20 %, following Poggie &

Porter (2019). The corresponding ratio of the leading shock to free stream velocity is presented in figure 13(b) across the different back pressures. It can be observed that whereas a coincidence between the Strouhal number and the leading shock-to-free stream speed ratios is not observed, the differences between their values are less than 25 % across the different settings; furthermore, the ratio  $u_s/U_\infty$  lies within the 0.02–0.05 bound observed in other canonical SBLI units (see Gonzalez & Dolling 1993 for a compilation of the shock speeds).

Evidently, the overall spectral features of the pressure fluctuation PSDs beneath the leading shock sharply resemble the separation shock oscillations in canonical (single shock) 2-D SBLI units. However, a notable difference is observed in the magnitude of the  $f_c$  in the present study compared with other 2-D SBLI units. Erengil & Dolling (1991), for example, reported that the shock zero crossing frequency was  $0.12U_\infty/\delta$  in their compression ramp interactions, which held constant across different inviscid shock strengths; similar zero crossing frequency was also reported in Gonzalez & Dolling (1993). By contrast, the  $f_c$  obtained in the present configuration is an order of magnitude lower and shows a decreasing trend with increasing back pressure. The substantially lower  $f_c$  is because the leading shock maintains a near-constant velocity during its unsteady motions at a speed of 3 %  $U_\infty$  that is very similar to canonical 2-D SBLI units. Since the intermittent length  $L_i$  of the leading shock of the present study is significantly larger compared with the canonical SBLI units available in the literature, the zero crossing frequency of the leading shock is consequently lower. Therefore, the observations suggest that the unifying parameter between the leading shock of the present study and the canonical SBLI is the constant shock speed, which is consistent with the arguments made by Clemens & Narayanaswamy (2014). For the remaining discussions, these broadband low frequency oscillations will be referred to as ‘SBLI’ modes.

Given the strong similarity in the Strouhal number scaling between the present and the canonical SBLI units, the Strouhal number based on  $L_i$  (from figure 9) and the peak frequency of the pressure oscillation PSD (from figure 13a) were used to estimate the corresponding separation scale,  $L_{sep}$ , of the leading shock at different back pressures. A strong caveat should be exercised that no additional off-surface visualization or measurements were made to evaluate the calculated  $L_{sep}$  at the exact jet injection pressures. Furthermore, prior works have shown the existence of multiple separation bubbles within the shock train and have argued that the shock train dynamics exhibit significant deviations from a canonical SBLI (Hunt & Gamba 2019). Therefore, in the present work, the  $L_{sep}$  is treated as an equivalent separation scale that can drive the leading shock if the leading shock unit resembled a canonical SBLI unit; the results presented so far support a strong resemblance. To alleviate the risk of using the estimated  $L_{sep}$  as a representative separation scale, the separation scale obtained using the surface streakline imagery at two intermediate jet injection pressures are compared with the estimated  $L_{sep}$  trend. The intermediate pressures were also used to evaluate (and establish) the continuing trend of the separation scales even at the intermediate back pressures other than the ones that are extensively reported in this work. Figure 14 presents the equivalent  $L_{sep}$  estimates at different back pressures. A remarkable agreement is observed between the estimated  $L_{sep}$  and the separation scale based on the streakline imagery at intermediate jet injection pressures. The  $L_{sep}$  exhibits over a four-fold increase in size between  $0.47D$  and  $2.24D$  over the back pressure range; based on the reference boundary layer thickness measured at  $x/D = 6.33$ , the  $L_{sep}/\delta$  is between 4.16 and 19.86. From Clemens & Narayanaswamy (2014), these separation scales belong to the size range where the separation shock motions are driven by the inherent pulsations of the downstream separated flow with only a modest direct contribution from the upstream boundary layer. If the  $p_b/p_\infty = 8.8$  case Strouhal

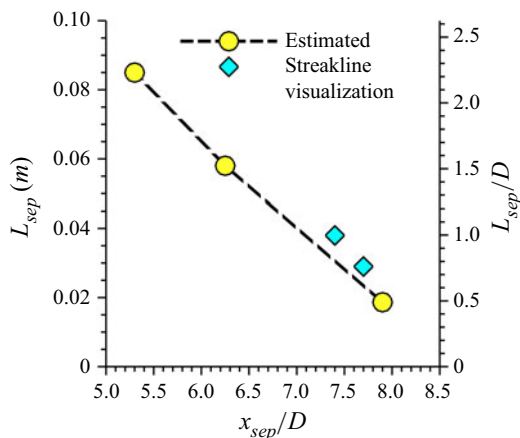


Figure 14. Estimated separation length scale  $L_{sep}$  for the different jet injection back pressures implemented in the present work. The separation scale is presented both in physical units as well as in terms of the isolator inner diameter. The measured  $L_{sep}$  from surface streakline imagery at intermediate jet injection pressures are also included in the figure.

number is assumed for  $p_b/p_\infty = 10.0$ , the corresponding  $L_{sep}$  is estimated at  $2.2D$  based on the peak frequency of the wall pressure fluctuation PSD of [figure 13\(a\)](#).

### 3.6. Spatiotemporal organization of pressure fluctuations

The spatiotemporal organization of the wall pressure fluctuation PSD is addressed as a first step to understanding the mechanisms that drive the leading shock pulsations. The frequency premultiplied PSDs were normalized by the  $p_{rms}^2$  to portray the relative PSD contributions at different frequencies within the pseudoshock region. The PSDs were obtained as an average over  $-50^\circ < \phi < +50^\circ$ . [Figure 15](#) presents the PSD evolution along the streamwise direction spanning the entire measurement domain and across different back pressure settings. The upstream boundary layer exhibits a monotonically increasing trend across all back pressures in [figure 15\(a–c\)](#). The unperturbed baseline isolator shock trains are also identified for  $p_b/p_\infty = 6.8$  ([figure 15a](#)) and  $p_b/p_\infty = 8.0$  ([figure 15b](#)) settings and their PSDs are quantitatively identical to those of the tare conditions discussed in [figure 12](#). Subsequently, the PSD shows a strong departure to dominant low frequency content beneath the leading shock, which was discussed in [figure 13](#). The distance over which the dominant low frequency content occurs is consistent with the intermittent region length across all back pressures.

The PSDs downstream of the leading shock show an immediate dominance of high-frequency content for  $p_b/p_\infty = 6.8$  to  $p_b/p_\infty = 8.8$  settings in [figure 15\(a–c\)](#). Such high-frequency content has been reported beneath the separated flow of canonical SBLI units and these frequencies are predominantly contributed by the shear layer eddies that develop over the separation bubble ([Chandola et al. 2017](#)). It should be noted that the present measurements cannot resolve the peak frequency of these pressure oscillations because they occur well above the Nyquist limit of the measurements. The PSD field at  $p_b/p_\infty = 8.8$  also reveals distinct bands of elevated frequencies within the shock train; these are annotated as ‘higher shock oscillation modes’ in [figure 15\(c\)](#). The dashed lines that correspond to the peak  $p_{rms}/p_w$  of the successive trailing shock feet are also presented in [figure 15\(c\)](#) to locate these frequency bands in relation to the trailing shocks. It is observed that successive shock feet exhibit a consistent increase in the frequency bands

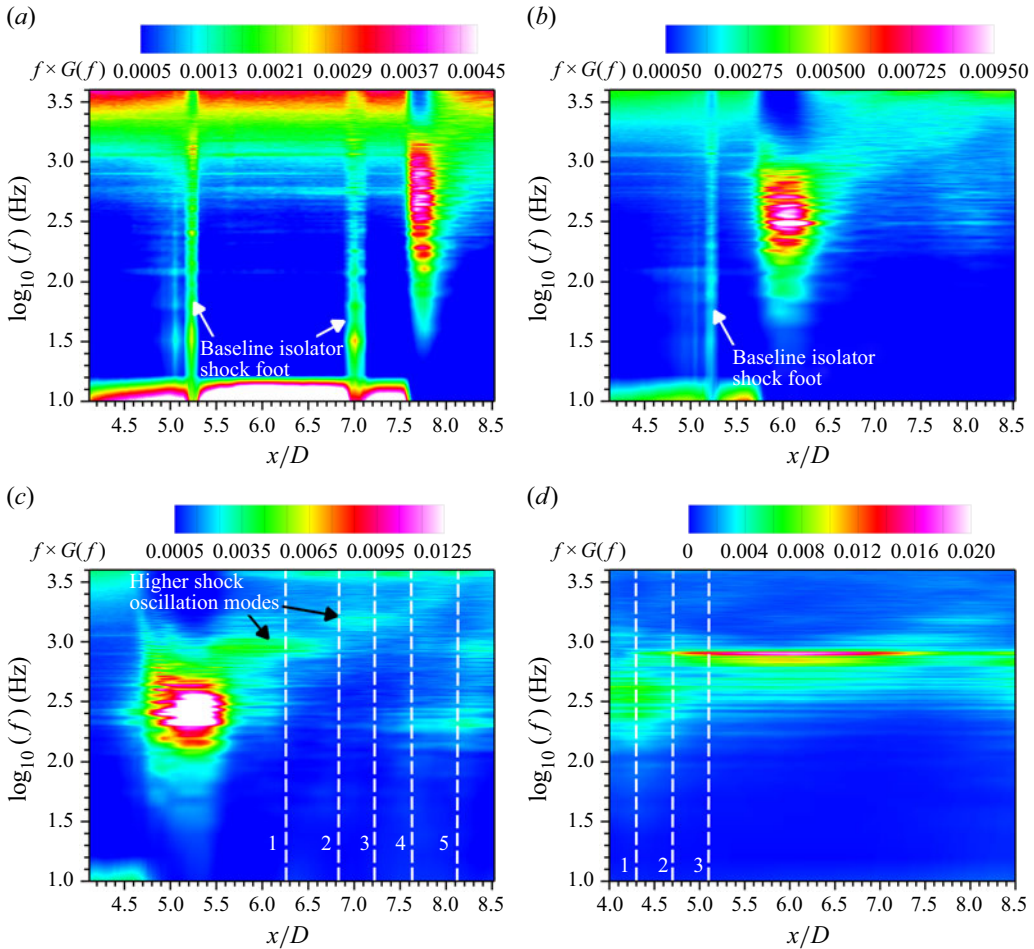


Figure 15. Evolution of PSD of the pressure fluctuations along the isolator section averaged over azimuthal region  $-50^\circ < \phi < +50^\circ$ . Four different test cases are presented: (a)  $p_b/p_\infty = 6.8$ ; (b)  $p_b/p_\infty = 8.0$ ; (c)  $p_b/p_\infty = 8.8$ ; (d)  $p_b/p_\infty = 10.0$ .

of oscillations until shock 4. Interestingly, shock 4 and shock 5 exhibit a prominent low frequency band whose frequency aligns closely with the SBLI mode of the leading shock; furthermore, shock 5 exhibits another frequency band that coincides with the higher shock oscillation mode of trailing shock 1. A similar but much weaker reemergence of SBLI mode frequencies of the leading shock oscillations can also be observed in  $p_b/p_\infty = 8.0$  at  $x/D \approx 8.1$ . Based on the  $L_{sep}$  estimates, the first three trailing shock feet that were identified in the  $p_{rms}/p_w$  profiles of  $p_b/p_\infty = 8.8$  are located within the separation bubble extent. Further, the location of the reemergence of the SBLI mode frequencies occurs just downstream of the estimated separation bubble scale for both back pressures in both  $p_b/p_\infty = 8.0$  and  $p_b/p_\infty = 8.8$  cases.

The PSDs of the trailing shocks of the  $p_b/p_\infty = 10.0$  case, presented in figure 15(d), reveal interesting similarities and departures from the jet injection cases. The first trailing shock exhibits a broadband bimodal PSD. At the lower frequencies, the PSD content is very similar to the SBLI mode of the leading shock PSD with a broad peak at approximately 300 Hz. This broad peak is followed by a minimum and another sharper



peak at approximately 840 Hz. This bimodal structure persists through the trailing shocks 2 and 3, and the contribution from the 840 Hz strengthens with distance while the low frequency band at 300 Hz weakens. Downstream of shock 3, the PSD continues to be broadband, but the frequency content at 840 Hz dominates the remaining frequencies resulting in a more tonal nature of the pressure oscillations over the majority of the measurement domain. Higher resonances of the baseline 840 Hz can also be observed between  $7.2 \leq x/D \leq 8.0$ , but their strengths are substantially lower than the baseline frequency. It is also interesting to note that the 840 Hz peak also penetrates upstream of the trailing shock 1 a little into the intermittent region of the leading shock. In fact, the pressure fluctuation PSD obtained within the intermittent region exhibit a very minor peak at 840 Hz and a notable tonal peak at 1200 Hz, as seen in [figure 13\(a\)](#). The nearly tonal nature of the pressure fluctuations suggests the acoustic origins of these frequency bands. Therefore, this frequency band and its resonances will be referred to as ‘acoustic’ modes. Comparing the higher shock oscillation modes of the  $p_b/p_\infty = 8.8$  case ([figure 15c](#)) with the acoustic mode of the  $p_b/p_\infty = 10.0$  case in [figure 15\(d\)](#), it can be observed that the fundamental acoustic mode frequency of the  $p_b/p_\infty = 8.8$  case at 840 Hz observed in trailing shock 1 corresponds very closely to the fundamental acoustic mode of the  $p_b/p_\infty = 10.0$  case, and the higher-order acoustic modes observed in trailing shocks 2, 3 and 4 are also observed in the downstream isolator section with  $p_b/p_\infty = 10.0$  ( $x/D > 7$ ). Interestingly, the strengths of these modes with  $p_b/p_\infty = 8.8$  are much weaker compared with the  $p_b/p_\infty = 10.0$  case and the occurrence of multiple acoustic resonances in the  $p_b/p_\infty = 8.8$  case contrasts the dominant occurrence of the fundamental mode in the cone injection.

Overall, a rather complex spatial distribution of the wall pressure fluctuations PSD is observed that exhibits both agreements and deviations from the prior works on shock train dynamics in planar isolators. The first point of consistency is the appearance of higher oscillation modes within the shock train that was also reported by Ikui *et al.* (1974b) and Hunt & Gamba (2019). The present work reveals a staggered increase in the acoustic mode frequencies for the  $p_b/p_\infty = 8.8$  case that is consistent with Hunt & Gamba (2019). However, the re-emergence of the low frequency content at a downstream distance observed in trailing shocks 4 and 5 of  $p_b/p_\infty = 8.8$  was not reported in the earlier works, which could be due to inadequate measurement stations at these locations in their works and/or differences in the pressure dynamics in the downstream regions. Second, it is evident that the dynamics of the regions upstream of the leading shock is unaltered by the pseudoshock, which was reported by Xiong *et al.* (2017).

The point of debate the present observations raise is the strong adherence of the leading shock dynamics to a canonical 2-D SBLI unit in terms of the Strouhal number scaling and the shock speed. Hunt & Gamba (2019) correctly pointed out that the acoustic modes do not occur in a canonical 2-D SBLI unit. Furthermore, Hunt & Gamba (2019) demonstrated a strong deviation in the peak Strouhal number (based on  $L_{sep}$ ) of the shock train oscillations compared with a canonical 2-D SBLI; in their study, the pressure fluctuation beneath the leading shock peaked at a Strouhal number of 0.56, which is significantly higher than canonical 2-D SBLI units. The present study, however, exhibits strong similarities between the leading shock dynamics and canonical 2-D SBLI dynamics in terms of the peak Strouhal number of the pressure fluctuation PSD. A major differentiating influence in the planar inlets arises from the junction and sidewall separations, which are absent in the present axisymmetric isolators. Therefore, the fundamental question is if the shock train dynamics are indeed governed by mechanisms similar to a canonical 2-D SBLI when it is devoid of the junction and the sidewall influences. It should be noted that Hunt & Gamba (2019) indeed point to the influence of the primary separation towards driving the leading



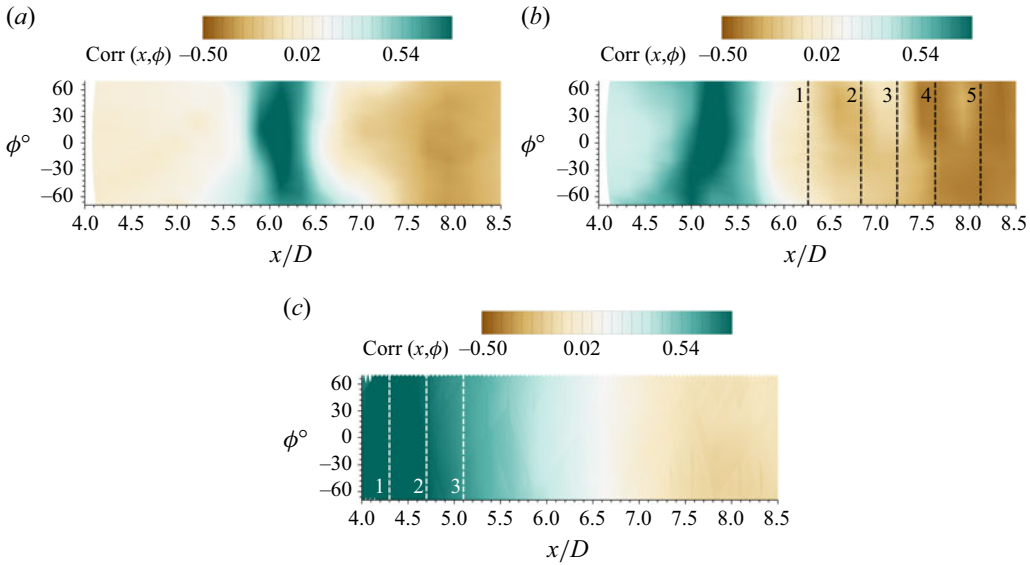


Figure 16. Two-dimensional maps of zero-lag cross-correlation coefficient of the pressure fluctuations within the isolator section with intermittent region as the reference location. Three different test cases are presented: (a)  $p_b/p_\infty = 8.0$ , jet injection; (b)  $p_b/p_\infty = 8.8$ , jet injection; (c) cone injection.

shock pulsations in planar isolators; the question is if the primary separation dynamics take a greater dominant role when the junctions/sidewall contributions cease to exist.

It should be remarked that without back pressure application, the shock oscillations have a very different signature and spectrum. The shock dynamics of tare operation have been reported and analysed in Leonard & Narayanaswamy (2021) for the specific case of the absence of shock-induced separation. It was shown that the shock train oscillations were dominated by frequencies that are over an order of magnitude lower than the frequencies with shock induced separation (also see figure 12). Furthermore, the mechanism driving these oscillations was suggested to be the phase lag of shock oscillations induced by the wall shear. By contrast, with back pressure deployment, the dynamical content and the driving interactions of the SBLI with back pressure are distinct from that of the tare operation, as will be expounded subsequently.

### 3.7. Cross-correlation analysis

#### 3.7.1. Zero-lag correlation fields

The zero-lag cross-correlation fields are analysed to determine which regions instantaneously correlate to the leading shock motions. A further objective is to evaluate the azimuthal extent over which the pressure fluctuations are correlated, which provides a clearer indication of the two-dimensionality of these interactions. Figure 16(a,b) present the zero-lag cross-correlation coefficient ( $\text{Corr}(x, \phi)$ ) fields with the reference location beneath the leading shock corresponding to peak  $p_{rms}/p_w$  and azimuthal centre ( $\phi = 0^\circ$ ) for  $p_b/p_\infty = 8.0$  and  $p_b/p_\infty = 8.8$ , respectively. A spanwise extended band of high  $\text{Corr}(x, \phi)$ , exceeding 0.7, is observed to extend across the azimuthal domain and over the intermittent region. This is immediately followed by a narrow band of near zero  $\text{Corr}(x, \phi)$  that once again extends across the azimuthal domain. This band is followed by a region of negative  $\text{Corr}(x, \phi)$  that extends until the end of the measurement domain. Whereas the  $\text{Corr}(x, \phi)$  is nearly uniform at  $p_b/p_\infty = 8.0$ , a modulation in the magnitude of

$\text{Corr}(x, \phi)$  was observed with  $p_b/p_\infty = 8.8$ . Juxtaposing the trailing shock feet locations at  $p_b/p_\infty = 8.8$  (figure 16b) reveals that the modulations are likely contributed by the coupling of leading shock with trailing shock motions. These bands are extended along the azimuthal direction covering most of the azimuthal domain. Interestingly, the trailing shock 4 and shock 5 that exhibited a PSD band in the SBLI mode show a remarkably higher negative correlation compared with the other trailing shocks.

The  $\text{Corr}(x, \phi)$  in the incoming boundary layer exhibits interesting differences between  $p_b/p_\infty = 8.0$  and  $p_b/p_\infty = 8.8$ . A very modest correlation between the leading shock and the incoming boundary layer that extends over the entire azimuthal region is observed for  $p_b/p_\infty = 8.0$ . This modest correlation is expected because of the large separation size, wherein the direct influence of the incoming boundary layer fluctuations towards driving the separation shock motions is minimal. However, the  $\text{Corr}(x, \phi)$  exhibits a noticeably higher value at  $p_b/p_\infty = 8.8$ . This elevated correlation is possibly because the leading shock motions influence the baseline isolator shock located at  $x/D = 3.6$  and pressure fluctuations in the region in between the shocks. It should be noted that a similar coupling was not observed with  $p_b/p_\infty = 8.0$  despite the upstream baseline isolator shock at  $x/D = 5.0$  being located at a similar distance from the leading edge of the pseudoshock. As such we do not have a clear explanation for the differences noted in the correlations with the upstream boundary layer. Overall, the leading shock motions at both back pressures presented are strongly influenced by the downstream separation and the ensuing downstream flow. The azimuthal spread of the  $\text{Corr}(x, \phi)$  reveals that the pseudoshock motions are correlated over the entire circumference, which suggests that the pseudoshock motions resemble a 2-D unit.

Figure 16(c) presents the corresponding zero-lag correlation with  $p_b/p_\infty = 10.0$  for a reference location at  $x/D = 4.0$ , which is within the intermittent region of the leading shock of the pseudoshock. Similar to the jet injection cases, a strong positive correlation was observed in the vicinity of the intermittent region across the entire azimuthal extent. This strong positive correlation also extends to the successive trailing shocks. In fact, it will be revealed in the subsequent discussions that the positive correlation extends over the entire isolator section even though the zero-lag correlation shows negatively correlated regions for  $x/D > 7$ . Thus, the entire flow field within the isolator section is highly coupled for the  $p_b/p_\infty = 10.0$  case, which is starkly different from the two jet injection cases discussed above.

### 3.7.2. Streamwise evolution of cross-correlation

The cross-correlation fields,  $\text{Corr}(x, \tau)$ , across different lags are presented to provide an understanding of how the pressure fluctuations are temporally organized within the pseudoshock region. Knowledge of the regions that lead and lag a given reference location will help identify the occurrence of disturbance nodes that can feed the leading shock oscillations and ultimately shed light on the mechanisms that drive the shock oscillations. The reference location for the jet injection cases is at the peak  $p_{rms}$  location of the leading shock of the pseudoshock and at  $x/D = 4.0$  for the  $p_b/p_\infty = 10.0$  case.

Figure 17 presents the cross-correlation field averaged over  $-50^\circ \leq \phi \leq +50^\circ$  along the measurement domain. Line contours of  $\text{Corr}(x, \tau)$  are included in each figure to delineate the regions of positive, negative and weak correlations. The locations of the trailing shocks are also annotated in figure 17(b,c). The overall cross-correlation field at a given time lag in the vicinity of  $\tau = 0$  ms resembles the zero-lag correlations in terms of the locations that are positively and negatively correlated. Beginning with the  $\text{Corr}(x, \tau)$  in the incoming boundary layer that is observable in figure 17(a), it is seen

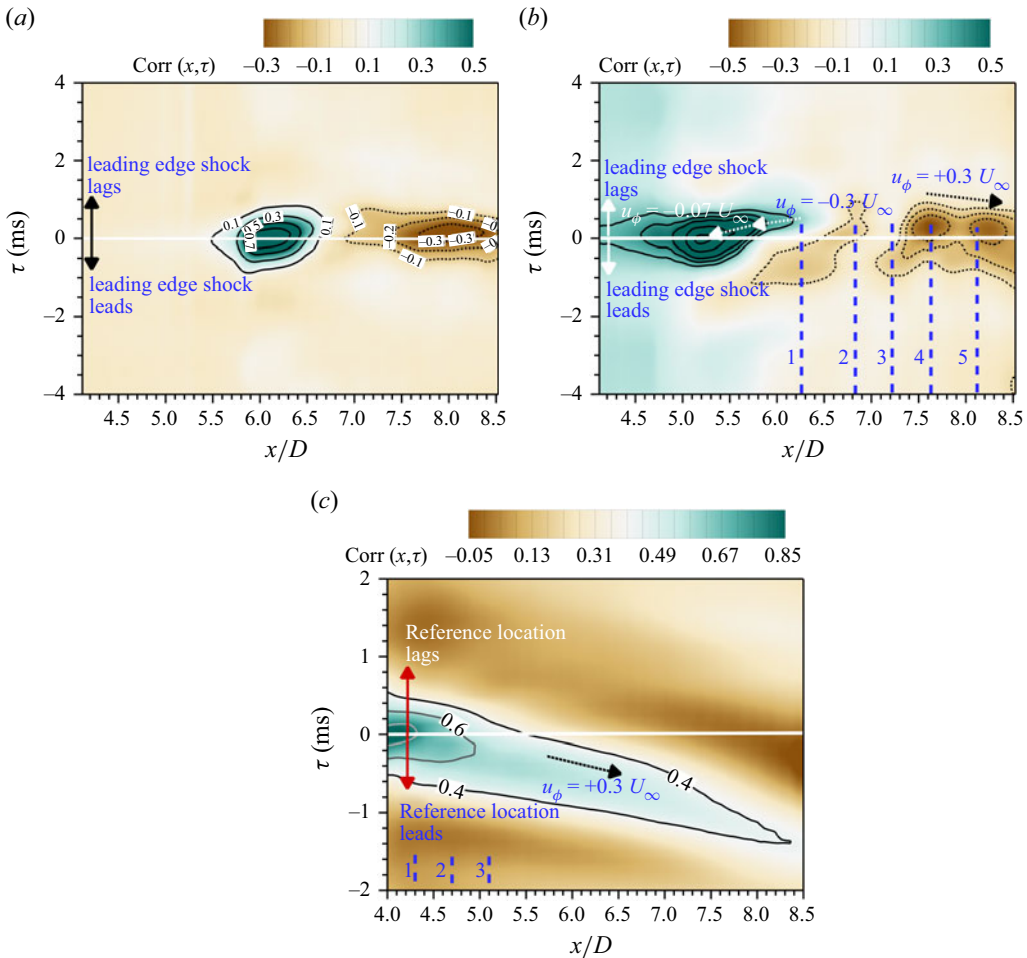


Figure 17. Evolution of cross-correlation coefficient of the pressure fluctuations along the isolator section with the intermittent region as the reference location. Three different test cases are presented: (a)  $p_b/p_\infty = 8.0$ , jet injection; (b)  $p_b/p_\infty = 8.8$ , jet injection; (c) cone injection.

that the value of  $\text{Corr}(x, \tau) \approx -0.1$  across all time lags. This suggests only a modest direct contribution from the incoming boundary layer towards driving the leading shock oscillations. This trend is expected to hold for the higher back pressure settings as well. A sharp increase in the  $\text{Corr}(x, \tau)$  can be observed within the intermittent region of the leading shock where the  $\text{Corr}(x, \tau)$  assumes high positive values. Tracking the location of the peak correlation in figure 17(a) reveals that the peak correlation magnitude occurs increasingly earlier with downstream distance; this corresponds to the occurrence of upstream propagating perturbations within the intermittent region. The progression of the time delay of the peak correlation provides a phase speed of  $u_\phi \approx 0.07u_\infty$  within the intermittent region ( $x/D \approx \pm 0.3$  surrounding the reference location) for both  $p_b/p_\infty = 8.0$  and  $p_b/p_\infty = 8.8$  settings. The phase speed is computed using the standard definition as the inverse of the difference in the time lag between the reference location and a given station of interest divided by the distance between the two locations. This phase speed is approximately a factor of two higher than the shock foot speed, but is very similar to the values reported in other works on canonical SBLI (Jenquin *et al.* 2023). The upstream

propagating perturbation continues to be present within of the separated flow and the propagation speed of the perturbations increases to  $u_\phi \approx 0.3u_\infty$  downstream into the separation bubble (e.g.  $x/D \leq 6.3$  in [figure 17b](#)). Farther downstream at  $x/D \approx 7.5$  in [figure 17\(b\)](#), the pressure perturbation changes into a downstream propagating perturbation with a propagation velocity of  $u_\phi \approx 0.3u_\infty$ ; this downstream propagating perturbation continues until the downstream end of the measurement domain. Within this downstream propagating perturbation region, distinct increases in the  $\text{Corr}(x, \tau)$  can be observed beneath the foot of trailing shocks 4 and 5, which exhibited notable overlap in the PSD with the intermittent region PSD. Overall, the cross-correlation fields reveal that the pressure fluctuations at  $x/D \approx 7.0$  within the separated flow lead all other locations within the pseudoshock for  $p_b/p_\infty = 8.8$  jet injection case and  $x/D \approx 6.5$  for  $p_b/p_\infty = 8.0$  jet injection case. This is evidence of the presence of a node in the vicinity of the reattachment location that originates the pressure perturbations that drive the leading shock motions.

The corresponding cross-correlation field for the  $p_b/p_\infty = 10.0$  case reveals that the intermittent region assumes a high positive  $\text{Corr}(x, \tau)$ . This positive  $\text{Corr}(x, \tau)$  extends over the bulk of the isolator, including the separated regions of the duct. Tracking the peak correlation once again reveals a downstream propagating perturbation with velocity  $u_\phi \approx 0.3u_\infty$ , which extends along the entire length of the measurement domain. Interestingly, in addition to the strong positive  $\text{Corr}(x, \tau)$ , a weak  $\text{Corr}(x, \tau)$  can also be observed extending along the length of the isolator. This perturbation is also observed to propagate downstream at a similar phase velocity as the positive  $\text{Corr}(x, \tau)$ . Importantly, unlike the lower back-pressure cases, a clear node within the separated flow that emanates upstream propagating perturbations into the leading shock cannot be located in the  $p_b/p_\infty = 10.0$  case.

### 3.7.3. Phase relation between the pressure fluctuations

The strong differences in the cross-correlation fields between the  $p_b/p_\infty \leq 8.8$  and  $p_b/p_\infty = 10.0$  cases discussed above raise the question if the leading shock is driven by different mechanisms in these two situations. An important reason for this perceived disparity is that the cross-correlation analysis provides the coupling information averaged over the entire frequency domain without delineating the individual SBLI and acoustic modes. The spectral phase lag analysis will offset this important limitation of the cross-correlations and help individually address the sources driving the SBLI and acoustic modes of the leading shock dynamics. The phase angle between the pressure fluctuations beneath the intermittent region of the leading shock (set as reference) and other locations within the isolator is presented in [figure 18](#) for the  $p_b/p_\infty = 8.8$  ([figure 18a](#)) and the  $p_b/p_\infty = 10.0$  cases ([figure 18b](#)). The reference locations chosen were identical to those previously employed for the cross-correlation analyses. In [figure 18](#), a positive phase delay would correspond to the pressure fluctuations at a given location within the isolator leading the intermittent region. Furthermore, the phase delay magnitude directly relates to the time delay at a given frequency. The locations of the trailing shock feet are labelled in [figure 18\(a,b\)](#) and the frequency corresponding to the fundamental acoustic mode is labelled by a solid horizontal line in each figure. In addition, [figure 18\(c\)](#) presents the corresponding line plots of the phase delay along the isolator section averaged over  $-50^\circ < \phi < +50^\circ$  and over  $95 \text{ Hz} < f < 500 \text{ Hz}$  for the SBLI mode, and  $830 \text{ Hz} < f < 850 \text{ Hz}$  for the acoustic mode.

For the jet injection case presented in [figure 18\(a\)](#), the frequency content in the intermittent region PSD corresponding to the SBLI mode made a dominant contribution to the PSD while the acoustic modes made only a weak contribution. Consistent with

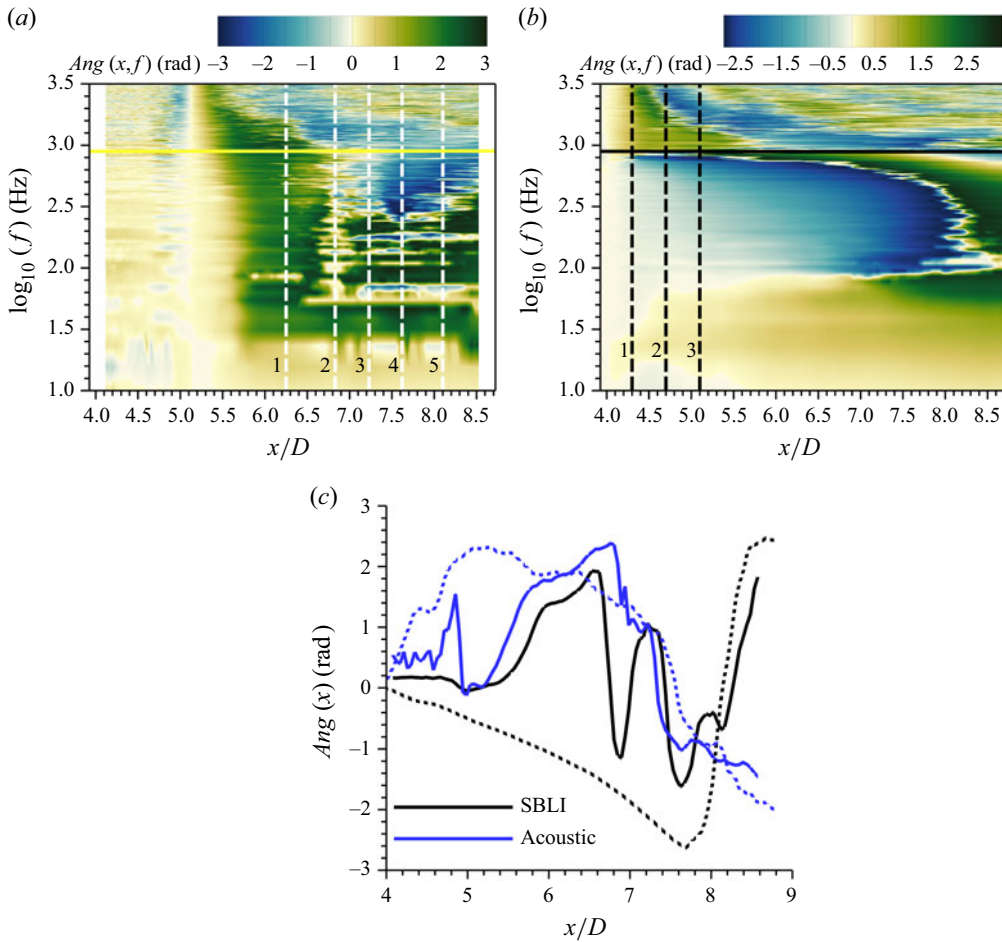


Figure 18. Spectral distribution of the phase angle of the pressure fluctuations within the isolator section with the intermittent region as the reference location. Two different cases are presented: (a)  $p_b/p_\infty = 8.8$ , jet injection; (b) cone injection. The corresponding line plots of the phase angle are presented (c) for  $p_b/p_\infty = 8.8$  (solid line) and  $p_b/p_\infty = 10.0$  (dashed line) for the SBLI and acoustic modes.

the cross-correlation lag analyses, the phase delay map portrays that pressure fluctuations within the separated flow lead the intermittent region of the leading shock (positive phase delay) in the SBLI mode that spans  $1.0 \leq \log_{10}(f) \leq 2.5$ . Furthermore, the line plot of the phase lag for the SBLI mode increases with increasing downstream distance until approximately  $x/D \approx 6.6$  after which an overall decrease trend can be noted more clearly in figure 18(c). This again is consistent with the occurrence of a node within the separated flow from which the pressure perturbations originate. At the frequency corresponding to the acoustic mode (shown as a yellow line in figure 18a) there are regions within the downstream isolator section that lead and lag the intermittent region in a manner that is broadly similar to the trends observed in the SBLI mode. This trend is clearer in figure 18(c).

Figure 18(b) presents the phase delay spectrum for the  $p_b/p_\infty = 10.0$  case, where the pressure fluctuation PSD within the intermittent region still had major contributions from both SBLI but with a minor presence of the fundamental acoustic mode. It can be observed from figure 18(b) that bulk of the isolator section spanning  $x/D < 8.0$  lags the separation



shock pulsations and the magnitude of the phase lag increases with downstream distance in the SBLI mode (also seen in [figure 18c](#)). The latter is once again consistent with the dominant downstream propagating pressure perturbations that were observed in cross-correlation analyses. Unlike the jet injection case, a node in the pressure fluctuation could not be identified in the  $p_b/p_\infty = 10.0$  case for the SBLI mode. In other words, all the pressure perturbations in the SBLI mode appear to emanate from the leading shock. Examining the frequencies surrounding the acoustic mode, [figure 18\(b\)](#) reveals an abrupt change in the phase delay evolution. At this narrow frequency range, a significant region of zero and positive phase delay can be observed. [Figure 18\(c\)](#) further reveals a trend of increasing and decreasing phase delay versus distance in the acoustic mode, which shows that perturbations of the leading shocks are fed from within the pseudoshock region. Finally, the pressure fluctuations at the downstream end of the measurement domain  $x/D > 8$  leads the intermittent location for the SBLI mode for all back pressure settings. This contrasts the acoustic mode where the pressure fluctuations at the downstream end of the measurement domain lag the intermittent region for both cases. It should be pointed out that the phase lag information at the downstream regions of the isolator section in both [figure 18\(a\)](#) and [figure 18\(b\)](#) are quite noisy for frequencies above 1.5 kHz, which makes it ambiguous to point the trends at higher acoustic modes.

#### 3.7.4. Flow asymmetry effects on PSD and statistical coupling

There were obvious azimuthal variations in the  $p_{rms}/p_w$  field and the positive azimuth exhibited higher  $p_{rms}/p_w$  compared with negative azimuth. Even though the dynamical content and statistics reported were averaged over  $-30^\circ \leq \phi \leq +30^\circ$ , the results are expected to be biased over the locations of higher-pressure fluctuations. Also, the averaging did not include more outboard locations, especially the weaker pressure fluctuation regions of  $\phi \leq -30^\circ$ . This challenges the generality of the dynamic content of the shock train and the statistical analysis reported, and the conclusions about the driving mechanics of the shock train oscillations that will be drawn subsequently. Therefore, specific investigations were conducted to determine the azimuthal variations of the PSD of the surface pressure fluctuations and a select collection of important statistical quantities upon which further conclusions are based.

[Figure 19\(a–d\)](#) presents the frequency premultiplied PSD of the surface pressure fluctuations within the leading shock intermittent region and successive trailing shocks 1, 4 and 5, at multiple azimuthal locations; the corresponding back pressure setting was  $p_b/p_\infty = 8.8$ . The PSD for this chosen back pressure setting exhibits the contribution from the SBLI mode as well as acoustic mode beneath the leading and trailing shocks of the shock train. In all [figure 19\(a–d\)](#), the PSD at  $\phi = -60^\circ$  was scaled by 1.25 to match the other PSDs in the overall magnitude. It can be observed that the PSDs across all azimuths exhibit remarkable coincidence with one another over the entire frequency range measured. The PSDs of the leading shock intermittent region for all the azimuths exhibit both SBLI and acoustic modes, as shown in [figure 19\(a\)](#). Quantitatively, however, whereas the PSDs are coincident in the low frequency unsteadiness band (SBLI modes) across all azimuths in [figure 19\(a\)](#), the acoustic mode is relatively reduced at  $\phi = -60^\circ$ . This mild reduction in the acoustic mode strength is also present in the trailing shock 4 at  $\phi = -60^\circ$  ([figure 19c](#)), but is absent in the trailing shocks 1 and 5 ([figure 19b,d](#)), as well as trailing shocks 2 and 3 (not shown).

The spectral coherence between the pressure fluctuations at a reference location within the leading shock intermittent region between  $-10^\circ \leq \phi \leq +10^\circ$  and all other locations in the isolator was computed to evaluate any deviations in the coupling strengths in



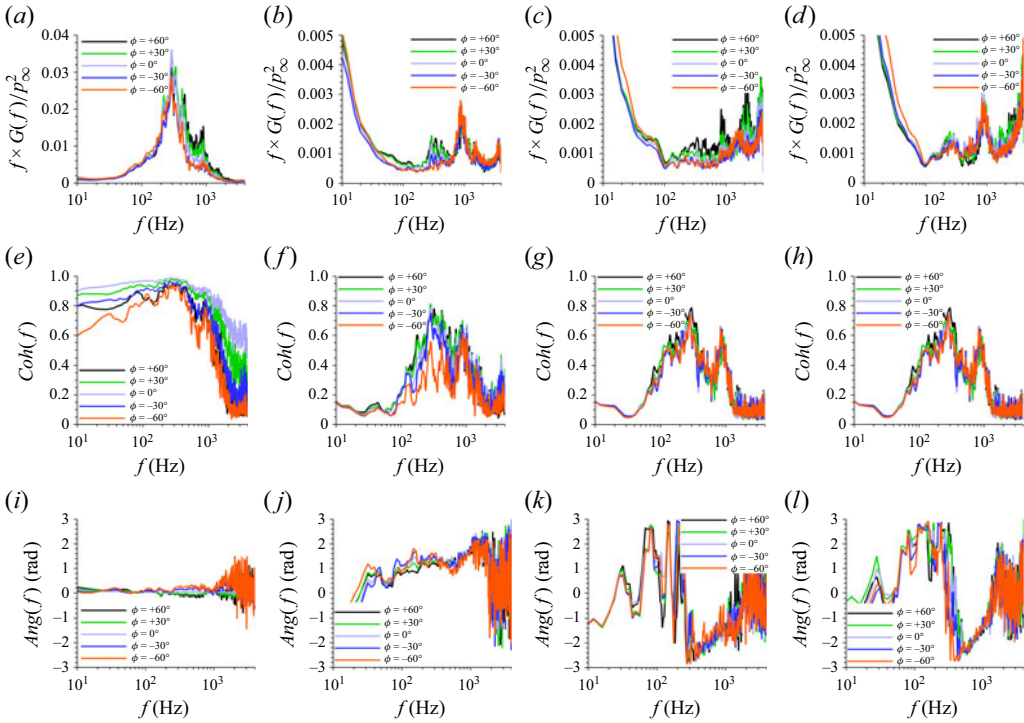


Figure 19. Evaluation of flow asymmetry on shock train dynamics and select statistical results at various locations within the shock train: (a–d) frequency premultiplied PSD beneath shock feet; (e–h) coherence magnitude at various locations within the shock train with reference location beneath the leading shock intermittent region; (i–l) corresponding phase delay spectra at various locations within the shock train. The shock train locations include: (a,e,i) leading shock intermittent region; (b,f,j) trailing shock 1; (c,g,k) trailing shock 4; (d,h,l) trailing shock 5. The results shown correspond to  $p_b/p_\infty = 8.8$  back pressure setting.

the azimuthal direction. Figure 19(e–h) presents the coherence within the leading shock intermittent region and the trailing shocks 1, 4 and 5 for  $p_b/p_\infty = 8.8$ . Once again, an excellent agreement in the coherence was obtained across all the azimuthal locations and within the shock train. The most deviation was observed at  $\phi = -60^\circ$  with a maximum difference of less than 0.2; this occurs in the leading shock intermittent region and trailing shock 1. The remarkable agreement in the coherence suggests that spectral coupling magnitude across the entire azimuthal domain is nearly identical and spans both the SBLI and acoustic modes that are of interest in the current work.

Finally, the phase angle between the pressure fluctuations at the same reference location and at all other locations within the shock train are presented in figure 19(i–l). Figure 19(i–l) presents the phase angle at the intermittent region, trailing shocks 1, 4 and 5, respectively. At the intermittent region, all azimuthal locations exhibit zero phase angle until 1 kHz and measurable excursions in the phase angle at higher frequencies (figure 19i). It should be noted that frequencies below 1 kHz encompass both the SBLI and acoustic modes. The zero phase angle illustrates that the entire leading shock oscillates in unison along the azimuthal direction, i.e. executes bulk shock motion. Similarly, all other trailing shocks execute in-phase oscillations along its azimuthal spread at a fixed phase delay from the reference location for this frequency range. This reinforces that each trailing shock of the shock train also oscillates in unison, thereby evidencing a bulk motion in the SBLI and acoustic modes of interest. These observations fortify that the dynamics and

statistical relationship in the shock train oscillations observed thus far by averaging over  $-30^\circ \leq \phi \leq +30^\circ$  are indeed representative of the entire azimuthal extent of the shock location. The weakening of shock foot at  $\phi \leq -30^\circ$  and the observed asymmetry in the  $p_{rms}/p_w$  does not influence the overall dynamical behaviour and coupling of the shock train in both SBLI and acoustic modes that are of interest in this work.

### 3.8. Discussions

The spectral trends and the corresponding correlation analyses reveal that a common feature of the shock oscillations across all jet injection cases is the occurrence of the SBLI mode of the leading shock that is driven by the separation bubble pulsations, which adheres to the description of a canonical SBLI unit despite the complications of the downstream separated flow within the pseudoshock. A clear node of pressure fluctuations is observed within the separated flow in the vicinity of the reattachment region for the SBLI mode, which is in conjunction with prior studies of canonical SBLI units (Chandola *et al.* 2017; Jenquin *et al.* 2023). A differentiating feature between the different cases is that whereas the acoustic modes are absent in the  $p_b/p_\infty = 6.8$  and  $p_b/p_\infty = 8.0$  cases, these oscillations occur at a low strength with  $p_b/p_\infty = 8.8$  and significantly higher strength with  $p_b/p_\infty = 10.0$ . The ensuing discussions will delve deeper into the origins of the acoustic modes, the reasons for their absence at low back pressures and the disparity in strength with changing back pressures.

A significant number of prior works pointed to the acoustic resonance that gets established within the isolator as a mechanism that drives the acoustic modes (Ikui *et al.* 1974a). An estimate for the resonance frequency has been suggested for transonic diffusers which are considered as an ideal organ pipe. The frequency  $f_n$  of a resonant mode  $n \in (0, 1, 2, \dots)$  is given by (Newsome 1984)

$$f_n = \frac{(2n+1)c}{4L}(1-M^2). \quad (3.1)$$

In the above equation,  $c$  is the speed of sound,  $L$  is the length of the diffuser and  $M$  is the Mach number downstream of the shock. Applying this equation for the present isolator results in the fundamental harmonic frequency  $f_0 = 205$  Hz for a limiting case of  $M = 0$ , and the value of  $f_0$  reduces further for a better estimate of  $M$ . This estimate is significantly lower than the observed fundamental acoustic mode frequency of 840 Hz. Similarly Sugiyama *et al.* (1988) suggested that the shock oscillations are driven by the acoustic wave that are set up between the leading pseudoshock and the duct exit. Applying this suggestion to the present study also yields inconsistent results; for example, this suggestion would lead to a substantial decrease in the shock/acoustic mode frequency between  $p_b/p_\infty = 8.8$  and  $p_b/p_\infty = 10.0$  cases, which was not observed in the present work. One can understand that the origin of the discrepancy is that these suggestions were intended for transonic diffusers where the flow downstream of the terminal shock is fully subsonic.

As such a feedback resonance within the entire duct is not feasible in the present study since the flow within the pseudoshock is not entirely subsonic. In fact, based on the wall pressure trace, the flow Mach number corresponding to the maximum mean static pressure recorded within the isolator remains supersonic for all the jet cases and subsonic only over a part of the isolator section for cone injection. For such situations, acoustic interactions can occur through the subsonic boundary layer region or within the limited cells of inviscid subsonic region when the shock train consists of normal shocks. In this context, the line plots of the phase delay presented in figure 18(c) provide a few interesting pointers. Considering the  $p_b/p_\infty = 8.8$  case, the location of peak positive

phase delay which corresponds to the node of pressure oscillations at  $x/D \approx 6.6$  for the SBLI mode and  $x/D \approx 6.8$  for the acoustic mode. Both these locations are in the close vicinity of the reattachment location, which was estimated at  $x/D \approx 7.3$  based on  $L_{sep}$  estimates. Similarly, considering the  $p_b/p_\infty = 10.0$  case, the node of pressure oscillations for the acoustic mode is located at  $x/D \approx 5.6$ . Going by the  $L_{sep}$  estimate of  $2.2D$  for the  $p_b/p_\infty = 10.0$  case based on the intermittent region PSD, and pinning the leading shock location to  $x/D = 3.75D$ , the node of the pressure fluctuation is once again located in the vicinity of the reattachment location of the separated flow downstream of the leading shock. Collating all the back pressure cases, it is clear that the node of the acoustic mode occurs within the separated flow in the vicinity of the reattachment region. However, if it is true that the acoustic modes are driven by the upstream propagating pressure fluctuations within the separated flow, then it stands to reason why acoustic modes were absent until  $p_b/p_\infty \leq 8.0$ , and only very weak oscillations were observed for  $p_b/p_\infty = 8.8$  compared with the  $p_b/p_\infty = 10.0$  case. A part of the reason could be the attenuation of the acoustic wave in supersonic boundary layers, as noted by Gawehn *et al.* (2010); however, this does not explain the total absence of the acoustic modes at lower back pressures whose magnitudes are still comparable to  $p_b/p_\infty = 8.8$ .

Robinet & Casalis (2001) theorized that the shock oscillations in transonic diffusers occur from feedback interactions between the acoustic waves that emanated at the reattachment location and the shock wave. These interactions are inviscid in nature, i.e. the viscous attenuations of the feedback acoustic waves do not change the nature of the outcome. Summarily, Robinet & Casalis (2001) hypothesized that the acoustic waves that are incident on a normal shock wave get reflected at different angles depending on their frequency. However, there exists a frequency for a given distance between the shock and the reattachment point where the reflected wave angle is the same as the incident wave angle; this coincidence results in a feedback amplification that can drive the leading shock oscillations. This angle is unique for a given Mach number upstream of the shock and the acoustic frequency, and is called the ‘critical angle’ in their work. Robinet & Casalis (2001) developed a 1-D stability analysis for a normal shock that is perturbed by an incident acoustic wave and demonstrated an excellent agreement with predicting the terminal shock oscillation frequencies of the transonic diffuser experiments of Bogar *et al.* (1983).

In the present study, we extended this analysis to delineate the predictions of this stability theory for the present experiments. Before the results are presented, multiple simplifications that were made by using this analysis need to be stated. First, the analysis was made for a 1-D flow problem, which is not the case in the present study. The main reason for not doing the stability analysis on the 2-D mean flow is the significantly higher computational cost that will be incurred. However, it is encouraging to observe the success of this analysis on transonic diffusers, where again the flow was not 1-D. Second, while the theory does not require a subsonic core flow downstream of the shock, the previous applications were made for transonic diffusers where the downstream core flow was indeed subsonic. As such there are no prior works that used the 1-D stability analysis on a supersonic isolator flow where the core flow is not subsonic. Third, while the inflow Mach number to the terminal (normal) shock of the transonic diffuser is well defined, it is not clear if we had to use the inflow Mach number upstream of the pseudoshock or the shock normal Mach number for making the estimate for the present case. With these caveats, it should be mentioned that the objective of the analysis is to unravel the underlying interactions that drive the shock train oscillations without seeking an exact quantitative agreement with the measured shock oscillation frequencies.

Figure 20 presents the leading shock oscillation (acoustic mode) frequency due to feedback shock–acoustic interactions over a range of separation lengths observed in the

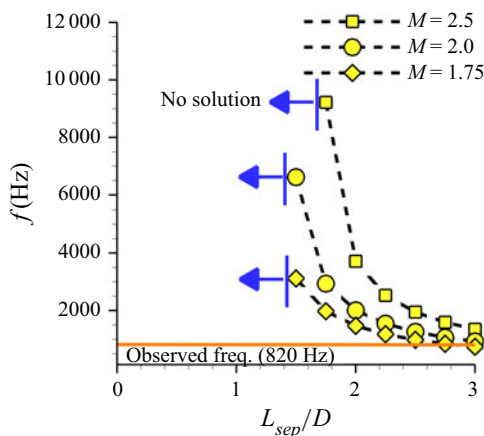


Figure 20. Most amplified acoustic mode frequency for different separation length scales over three different Mach numbers that correspond to the total and shock normal Mach numbers for  $p_b/p_\infty = 8.8$  and  $p_b/p_\infty = 10.0$  cases.

present experiments. Three different inflow Mach numbers were chosen. First,  $M = 2.5$  corresponds to the estimated Mach number upstream of the leading shock based on the isolator surface pressure just upstream of the pseudoshock and using oblique shock relations. Next,  $M = 2.0$  corresponds to an ‘effective’ shock normal Mach number based on the pressure at the estimated reattachment location of the  $p_b/p_\infty = 8.8$  case and the pressure upstream of the pseudoshock, and  $M = 1.75$  corresponds to the above estimate for the  $p_b/p_\infty = 10.0$  case. It can be observed from figure 20 that a solution to the feedback amplification does not exist for the separation size below a threshold for a given Mach number. This threshold value is  $L_{sep}/D \approx 1.6 - 1.8$  for the chosen Mach number range. This threshold occurs because below this separation size the critical angle criterion for any frequency cannot be accommodated within the spatial constraint posed by the distance between the shock wave and the reattachment point. Interestingly, the estimated  $L_{sep}$  for  $p_b/p_\infty = 6.8$  and  $p_b/p_\infty = 8.0$  were both below this threshold limit. Beyond the threshold  $L_{sep}$ , a sharply decreasing trend could be observed in the amplified frequency with increasing  $L_{sep}$ , where higher Mach numbers yield a higher frequency for a given  $L_{sep}$ . The divergence in the most amplified frequency across different Mach numbers considered sharply decreases with increasing  $L_{sep}$ ; for example, the spread is approximately 1.5 kHz for  $L_{sep} = 2.5D$ . The mean separation scale for  $p_b/p_\infty = 8.8$  and with  $p_b/p_\infty = 10.0$  were both estimated to be around  $2.3D$ ; at this separation scale, the most amplified frequency ranged between 1.2 kHz to 3 kHz for the different Mach numbers chosen. Given the separation shock oscillates over the intermittent region, which is approximately  $0.5D$ , the most amplified frequencies spreads over a range of values causing a spectral spread in the PSD. It should also be noted that for the approximations that were made with extending the 1-D analysis tool, this level of quantitative agreement is quite remarkable.

The analysis presented above makes several qualitatively consistent behaviours with the experimental observations and provides a platform to explain the mechanisms that drive the shock–acoustic interactions. Based on the above arguments, a picture emerges that the shock–acoustic interactions are most likely driven by inviscid interactions between the acoustic perturbations emanated at the reattachment point and the leading shock wave. An important requirement to have a positive feedback amplification is that the separation scales should be large enough to support an acoustic frequency and be incident on the

shock wave at its critical angle; this in turn requires a threshold back pressure to generate the shock–acoustic interaction modes. Furthermore, the unsteadiness of the separation bubble causes broadband oscillations of the separation scales and hence a spread in the most amplified frequency from the shock–acoustic interactions. Interestingly, [figure 20](#) shows that this spread in the most amplified acoustic mode frequency shrinks with increasing separation size for a given Mach number and also across different inflow Mach numbers upstream of the shock train leading edge. The manifestation of these features are observed across many other shock train dynamics studies, which was discussed in § 3.3.

It should be remarked that the self-excited oscillations should be understood in the context of the effective pressure ratio influencing the interaction. However, the shock train oscillations are driven by multiply coupled interactions during the pseudoshock processing of the flow field, which was expounded in considerable depth in this work. This challenges the objective quantification of the driving back pressure ratio. We, therefore, performed RANS simulations with different imposed uniform pressure boundary conditions at the isolator exit. The isolator exit pressure that best matched the leading shock foot location of the shock train between computations and experiments was reported as an effective back pressure that drives the shock train structure. It should be noted that this back pressure need not drive the shock train dynamics. As expounded in this work the effective back pressure that influences the interactions depends more directly on the separation scales at the different operation conditions and the occurrence of feedback shock–acoustic interactions. There is indeed an implicit relationship between this driving back pressure of the shock train dynamics determined by the separation scales and the isolator exit pressure.

The analysis presented above shows that there are two major mechanisms, separation bubble pulsations and shock–acoustic interactions, which coexist and mutually compete to drive the shock train oscillations. For low back pressure settings, e.g.  $p_b/p_\infty \leq 8.0$  in this study, the low frequency separation bubble pulsations are shown to dominate the shock train dynamics as observed from the PSD maps (see [figure 15a,b](#)) and the statistical analyses. With increasing back pressure, the shock–acoustic interactions make an increasing contribution above a certain threshold back pressure ( $p_b/p_\infty \approx 8.8$  in this study, see [figure 15c](#)) and makes a prominent contribution to the shock train oscillations at elevated back pressures, as shown in [figure 15\(d\)](#) obtained at  $p_b/p_\infty \geq 10.0$ . It is interesting to note that the computed flow fields of [figure 11](#) obtained at  $p_b/p_\infty = 8.8$  and  $p_b/p_\infty = 10.0$  reveal the presence of a subsonic mixing layer towards the isolator exit at this back pressures. Based on the dissipation of the trailing shocks, the mixing layer was traced to begin at  $x/D \approx 9.0$  for  $p_b/p_\infty = 8.8$  and  $x/D \approx 8.0$  for  $p_b/p_\infty = 10.0$ . While it is not clear if the occurrence of a subsonic mixing layer is a necessary criterion to observe the shock–acoustic interactions, the evidences strongly suggest that the extent of the subsonic mixing layer correlates with the strengthening of shock–acoustic feedback coupling in this study.

### 3.9. Relationship to other inlet/isolator geometry

The axisymmetric shock train dynamics presented in this article have direct logical relationship and extensions to the shock dynamics of high-efficiency self-starting hypersonic inlets. These inlets are typically axisymmetric in geometry and compress the inflow through an asymmetric shock train system. A number of recent works investigated the flow field and shock field within these high-efficiency inlets across different geometries and reported noteworthy similarities in the shock train oscillations and evolutionary trend with the current study. Johnson *et al.* (2022b) conducted an experimental investigation of the shock train dynamics within a back pressured axisymmetric truncated Busemann



inlet with a Mach 4 inflow and observed tonal oscillations of the shock foot leading edge peaking at  $\approx 1$  kHz overlaid on broadband motions at elevated back pressures. Similar observations were also made by Bustard *et al.* (2025) in an oscillating waverider inlet subject to back pressure. Recently, Schram *et al.* (2025b) investigated the axisymmetric truncated Busemann inlet subject to back pressures at negative incidence angle in a Mach 4 inflow. Once again, the authors observed a similar progression of the shock train leading-edge oscillations from broadband oscillations to tonal oscillations at  $\approx 1$  kHz. Furthermore, Baccarella *et al.* (2021) studied the axisymmetric isolator shock train oscillations with back pressure imposed using mass addition and combustion that included two different flow enthalpy settings. The authors observed tonal oscillations of the isolator shock train above certain fuel equivalence ratio and mass addition thresholds, with the peak shock oscillations at a 400 Hz–1 kHz range. The consistency of the qualitative trending from broadband to tonal shock train leading-edge oscillations in these applied geometries reinforce that the transition in the driving mechanism pervades across various geometries. The rather close alignment in the tonal frequency across multiple studies spanning multiple Mach numbers and compression ratios supports the observation made from figure 20 that the acoustic mode frequency spread narrows over different inflow Mach numbers at large separation scales.

#### 4. Conclusions

The present work investigated the mechanisms that drive the pseudoshock motions within axisymmetric isolators across a wide range of back pressures. Over this back pressure range, the leading shock of the pseudoshock was located between  $x/D = 7.5$  to  $x/D = 3.75$ , spanning approximately 40 % of the isolator length. The resulting separated flow emanated by the leading shock is estimated to change by over five fold across the different back pressures. Upstream of the pseudoshock, the internal shock system within the inlet/isolator did not cause boundary layer separation and resulted in a nearly 2-D inflow into the pseudoshock. Therefore, the present unit makes one of the simplest academic configurations to study the pseudoshock dynamics by avoiding the strong 3-D interactions from the sidewalls and junctions that occur in planar inlet/isolator geometries.

High bandwidth 2-D pressure field imaging was performed at 8 kHz within the isolator for different back pressure settings. The acquisition rate was considerably higher than the dominant frequency of the shock train oscillations across the different back pressure settings. The PSD of the pressure fluctuation beneath the leading shock foot exhibited a low frequency broadband spectrum across all back pressures. With increasing back pressure, an additional peak occurred at a distinct higher frequency with a minimal spread in PSD around this peak frequency; this additional peak persisted within the entire pseudoshock. The cross-correlation analysis revealed that the low frequency broadband oscillations were caused by the separation bubble pulsations downstream of the leading shock. A node in the vicinity of the reattachment location from where the pressure perturbations that drive the separation shock oscillations was also identified for all back pressures. These observations reinforced that the low frequency pulsations indeed corresponded to low frequency pulsations reported in canonical SBLI units even though the separated flow in the pseudoshock region may contain additional complexities and modulations due to the trailing shocks of the shock train.

The higher frequency was found to be caused by shock interactions with the upstream propagating acoustic waves. Interestingly, none of the frequency scaling proposed that treated the isolators as traditional resonators made a notable agreement with the observed acoustic mode frequencies. Furthermore, these approaches could not capture the absence

of the acoustic modes at the low back pressure settings. The feedback interactions described using 1-D stability analysis of the shock interactions perturbed by upstream propagating acoustic waves from the reattachment locations was extended to the present work. The frequency that made a critical incidence to the shock wave was computed using the method developed by Robinet & Casalis (2001). It was observed that below a threshold separation scale of  $L_{sep} \approx 1.5\text{--}1.8 D$ , no frequency values could satisfy the critical incidence criterion. The existence of a threshold  $S_{sep}$  to generate the acoustic mode and the value of the threshold were highly consistent with the separation scales over which the acoustic modes were absent in the present work. Further, the most amplified acoustic mode frequency at the separation scales of higher back pressure settings of the present work also made a fair comparison with the experimentally observed frequencies. Overall, the evidence suggests that the leading shock of the pseudoshock is driven by the viscous interactions within the separation bubble for the low frequency broadband pulsations and inviscid shock–acoustic interactions for higher frequency narrow band oscillations.

**Acknowledgements.** This work was supported by ONR grant N00014-21-1-2005 with Dr D. Gonzalez and Dr L. Myers as programme managers.

**Declaration of interests.** The authors report no competing financial interests or personal relationships that could appear to have influenced the work reported in this paper. The authors report no conflict of interest.

#### REFERENCES

- BABINSKY, H. & HARVEY, J.K. 2011 *Shock Wave-Boundary-Layer Interactions*. vol. 32, Cambridge University Press.
- BACCARELLA, D., LIU, Q., MCGANN, B., LEE, G. & LEE, T. 2021 Isolator-combustor interactions in a circular model scramjet with thermal and non-thermal choking-induced unstart. *J. Fluid Mech.* **917**, A38.
- BOGAR, T.J., SAJBEN, M. & KROUTIL, J.C. 1983 Characteristic frequencies of transonic diffuser flow oscillations. *AIAA J.* **21** (9), 1232–1240.
- BUSTARD, A., NOFTZ, M.E., JEWELL, J.S. & JULIANO, T.J. 2025 Fast pressure-sensitive paint measurements of an internal oscillating waverider inlet unstarted by mass injection. In *AIAA SCITECH 2025 Forum*, pp. 0549. American Institute of Aeronautics and Astronautics.
- CARROLL, B.F., LOPEZ-FERNANDEZ, P.A. & DUTTON, J.C. 1993 Computations and experiments for a multiple normal shock/boundary-layer interaction. *J. Propul. Power* **9** (3), 405–411.
- CARROLL, B.F. & DUTTON, J.C. 1990 Characteristics of multiple shock wave/turbulent boundary-layer interactions in rectangular ducts. *J. Propul. Power* **6** (2), 186–193.
- CHANDOLA, G., HUANG, X. & ESTRUCH-SAMPER, D. 2017 Highly separated axisymmetric step shock-wave/turbulent-boundary-layer interaction. *J. Fluid Mech.* **828**, 236–270.
- CLEMENS, N.T. & NARAYANASWAMY, V. 2014 Low-frequency unsteadiness of shock wave/turbulent boundary layer interactions. *Annu. Rev. Fluid Mech.* **46** (1), 469–492.
- CRIST, S., GLASS, D.R. & SHERMAN, P.M. 1966 Study of the highly underexpanded sonic jet. *AIAA J.* **4** (1), 68–71.
- DUSSAUGE, J.-P. & PIPONNIAU, S. 2008 Shock/boundary-layer interactions: possible sources of unsteadiness. *J. Fluids Struct.* **24** (8), 1166–1175.
- EGAMI, Y., SATO, Y. & KONISHI, S. 2019 Development of sprayable pressure-sensitive paint with a response time of less than 10  $\mu$ s. *AIAA J.* **57** (5), 2198–2203.
- ERENGIL, M.E. & DOLLING, D.S. 1991 Unsteady wave structure near separation in a Mach 5 compression ramp interaction. *AIAA J.* **29** (5), 728–735.
- FERRI, A. & NUCCI, L.M. 1951 The origin of aerodynamic instability of supersonic inlets at subcritical conditions. *NACA Tech. Rep.* No. RM-L50K30. National Advisory Committee for Aeronautics.
- FUNDERBURK, M.L. & NARAYANASWAMY, V. 2019a Investigation of negative surface curvature effects in axisymmetric shock/boundary-layer interaction. *AIAA J.* **57** (4), 1594–1607.
- FUNDERBURK, M.L. & NARAYANASWAMY, V. 2019b Spectral signal quality of fast pressure sensitive paint measurements in turbulent shock-wave/boundary layer interactions. *Exp. Fluids* **60** (10), 1–20.
- GAWEHN, T., GÜLHAN, A., AL-HASAN, N.S. & SCHNERR, G.H. 2010 Experimental and numerical analysis of the structure of pseudo-shock systems in laval nozzles with parallel side walls. *Shock Waves* **20** (4), 297–306.

- GNANI, F., ZARE-BEHTASH, H. & KONTIS, K. 2016 Pseudo-shock waves and their interactions in high-speed intakes. *Prog. Aerosp. Sci.* **82**, 36–56.
- GONSALEZ, J. & DOLLING, D. 1993 Correlation of interaction sweepback effects on unsteady shock-induced turbulent separation. In 31st Aerospace Sciences Meeting, pp. 776. American Institute of Aeronautics and Astronautics.
- HEISTER, W.H. & PRATT, D.T. 1994 *Hypersonic Airbreathing Propulsion*. American Institute of Aeronautics and Astronautics.
- HOU, W., CHANG, J., XIE, Z., WANG, Y., WU, L. & BAO, W. 2020 Behavior and flow mechanism of shock train self-excited oscillation influenced by background waves. *Acta Astronaut.* **166**, 29–40.
- HSIEH, T., BOGAR, T.J. & COAKLEY, T.J. 1987 Numerical simulation and comparison with experiment for self-excited oscillations in a diffuser flow. *AIAA J.* **25** (7), 936–943.
- HUANG, H.-X. *et al.* 2023 A review of the shock-dominated flow in a hypersonic inlet/isolator. *Prog. Aerosp. Sci.* **143**, 100952.
- HUNT, R.L. & GAMBA, M. 2018 Shock train unsteadiness characteristics, oblique-to-normal transition, and three-dimensional leading shock structure. *AIAA J.* **56** (4), 1569–1587.
- HUNT, R.L. & GAMBA, M. 2019 On the origin and propagation of perturbations that cause shock train inherent unsteadiness. *J. Fluid Mech.* **861**, 815–859.
- IKUI, T., MATSUO, K. & MINORU, N. 1974a The mechanism of pseudo-shock waves. *Bull. JSME* **17** (108), 731–739.
- IKUI, T., MATSUO, K., MINORU, N. & MASANOBU, H. 1974b Oscillation phenomena of pseudo-shock waves. *Bull. JSME* **17** (112), 1278–1285.
- JENQUIN, C., JOHNSON, E.C. & NARAYANASWAMY, V. 2023 Investigations of shock–boundary layer interaction dynamics using high-bandwidth pressure field imaging. *J. Fluid Mech.* **961**, A5.
- JOHNSON, E., JENQUIN, C., MCCREADY, J., NARAYANASWAMY, V. & EDWARDS, J.R. 2022a Mach 4 performance of a hypersonic streamtraced inlet-part 1: experimental investigations. In AIAA SciTech 2022 Forum, pp. 0065. American Institute of Aeronautics and Astronautics.
- JOHNSON, E., JENQUIN, C. & NARAYANASWAMY, V. 2022b Experimental studies of unstart shock dynamics within a streamtraced scramjet inlet. In AIAA AVIATION 2022 Forum, pp. 3478. American Institute of Aeronautics and Astronautics.
- JOHNSON, E.C. & NARAYANASWAMY, V. 2024 High-bandwidth pressure field imaging of stream-traced inlet unstart dynamics. *AIAA J.* **62** (11), 4494–4499.
- LEONARD, M.D. & NARAYANASWAMY, V. 2021 Investigation of shock dynamics in an axisymmetric inlet/isolator with attached boundary layers. *J. Fluid Mech.* **908**, A42.
- LI, N., CHANG, J.-T., XU, K.-J., YU, D.-R., BAO, W. & SONG, Y.-P. 2017 Prediction dynamic model of shock train with complex background waves. *Phys. Fluids* **29** (11), 116103.
- MATSUO, K., MIYAZATO, Y. & KIM, H.-D. 1999 Shock train and pseudo-shock phenomena in internal gas flows. *Prog. Aerosp. Sci.* **35** (1), 33–100.
- MCMULLEN, R.M., HUYNH, D.P., GREGORY, J. & CRAFTON, J.W. 2013 Dynamic calibrations for fast-response porous polymer/ceramic pressure-sensitive paint. In AIAA Ground Testing Conference, pp. 3123. American Institute of Aeronautics and Astronautics.
- MEIER, G.E.A., SZUMOWSKI, A.P. & SELEROWICZ, W.C. 1990 Self-excited oscillations in internal transonic flows. *Prog. Aerosp. Sci.* **27** (2), 145–200.
- MORGAN, B., DURAISAMY, K. & LELE, S.K. 2014 Large-eddy simulations of a normal shock train in a constant-area isolator. *AIAA J.* **52** (3), 539–558.
- NEWSOME, R.W. 1984 Numerical simulation of near-critical and unsteady, subcritical inlet flow. *AIAA J.* **22** (10), 1375–1379.
- OH, J.Y., MA, F., HSIEH, S.-Y. & YANG, V. 2005 Interactions between shock and acoustic waves in a supersonic inlet diffuser. *J. Propul. Power* **21** (3), 486–495.
- OM, D., VIEGAS, J.R. & CHILDS, M.E. 1985 Transonic shock-wave/turbulent boundary-layer interactions in a circular duct. *AIAA J.* **23** (5), 707–714.
- OSWATITSCH, K.L. 1944 Der druckrückgewinn bei geschossen mit rückstossantrieb bei hohen über-schallgeschwindigkeiten (der wirkungsgrad vos stossdiffusoren). *Forschungen Und Entwicklung des Heereswaffenamtes* **1005**.
- PHILIPPOU, A.L., ZACHOS, P.K. & MACMANUS, D.G. 2024 Aerodynamic instabilities in high-speed air intakes and their role in propulsion system integration. *Aerospace* **11** (1), 75.
- PICKLES, J.D. & NARAYANASWAMY, V. 2020 Control of fin shock induced flow separation using vortex generators. *AIAA J.* **58** (11), 4794–4806.
- POGGIE, J. & PORTER, K.M. 2019 Flow structure and unsteadiness in a highly confined shock-wave–boundary-layer interaction. *Phys. Rev. Fluids* **4** (2), 024602.

- PUCKETT, S. & NARAYANASWAMY, V. 2024 High-bandwidth pressure field imaging of fin-generated shock wave–boundary layer interactions. *J. Fluid Mech.* **999**, A80.
- ROBINET, J.-C. & CASALIS, G. 1999 Shock oscillations in diffuser modeled by a selective noise amplification. *AIAA J.* **37** (4), 453–459.
- ROBINET, J.-C. & CASALIS, G. 2001 Critical interaction of a shock wave with an acoustic wave. *Phys. Fluids* **13** (4), 1047–1059.
- SCHRAM, M., STRAMECKY, W. & NARAYANASWAMY, V. 2025a Unstart Sensitivity of Hypersonic Streamtraced Inlets During Angle-of-Attack Operation. *AIAA J.* 1–10.
- SCHRAM, M.J., THILL, A. & NARAYANASWAMY, V. 2025b Unsteady shock dynamics in hypersonic streamtraced busemann inlet at sub-design mach number and varying angles of attack. In *AIAA SCITECH 2025 Forum*, pp. 0337. American Institute of Aeronautics and Astronautics.
- SUGIYAMA, H., TAKEDA, H., ZHANG, J., OKUDA, K. & YAMAGISHI, H. 1988 Locations and oscillation phenomena of pseudo-shock waves in a straight rectangular duct. *JSME Intl J. Ser. 2, Fluids Engng Heat Transfer Power Combust. Thermophys. Properties* **31** (1), 9–15.
- SULLINS, G.A. 1993 Demonstration of mode transition in a scramjet combustor. *J. Propul. Power* **9** (4), 515–520.
- SULLINS, G. & MCLAFFERTY, G. 1992 Experimental results of shock trains in rectangular ducts. In *AIAA 4th International Aerospace Planes Conference*, pp. 5103. American Institute of Aeronautics and Astronautics.
- SUN, C.-C. & CHILDS, M.E. 1976 Wall-wake velocity profile for compressible nonadiabatic flows. *AIAA J.* **14** (6), 820–822.
- VARIGONDA, S.V. & NARAYANASWAMY, V. 2021 Methodology to image the panel surface pressure power spectra in weakly coupled fluid/structure interactions. *Exp. Fluids* **62** (11), 1–17.
- WALTRUP, P.J. & BILLIG, F.S. 1973 Structure of shock waves in cylindrical ducts. *AIAA J.* **11** (10), 1404–1408.
- WALZ, J. & NARAYANASWAMY, V. 2023 Dual separation control and drag mitigation in high speed flows using viscoelastic materials. *Phys. Fluids* **35** (3), 031704.
- WEISS, A., GRZONA, A. & OLIVIER, H. 2010 Behavior of shock trains in a diverging duct. *Exp. Fluids* **49**, 355–365.
- WOOD, S.J., STEPHEN, S., JENQUIN, C., JOHNSON, E. & NARAYANASWAMY, V. 2023 Development and testing of high-temperature fast response pressure sensitive paint. In *AIAA SCITECH 2023 Forum*, pp. 1181. American Institute of Aeronautics and Astronautics.
- XIONG, B., WANG, Z.-G., FAN, X.-Q. & WANG, Y. 2017 Response of shock train to high-frequency fluctuating backpressure in an isolator. *J. Propul. Power* **33** (6), 1520–1528.
- YAMANE, R., KONDO, E., TOMITA, Y. & SAKAE, N. 1984a Vibration of pseudo-shock in straight duct: 1st report, fluctuation of static pressure. *Bull. JSME* **27** (229), 1385–1392.
- YAMANE, R., TAKAHASHI, M. & SAITO, H. 1984b Vibration of pseudo-shock in straight duct: 2nd report, calculation of static pressure fluctuation. *Bull. JSME* **27** (229), 1393–1398.